Digit. Signal Process. 156 (2025) 104781

Contents lists available at ScienceDirect

Digital Signal Processing

journal homepage: www.elsevier.com/locate/dsp

Quaternion optimized model with sparseness for color image recovery

Liqiao Yang [a,b], Yang Liu [c], Kit Ian Kou [d,*]

[a] School of Computing and Artificial Intelligence, Southwestern University of Finance and Economics, Chengdu 611130, China
[b] Research Institute for Digital Economy and Interdisciplinary Sciences, Southwestern University of Finance and Economics, Chengdu, 611130, China
[c] College of Mathematics and Computer Science and the College of Mathematical Medicine, Zhejiang Normal University, Jinhua 321004, China
[d] Department of Mathematics, Faculty of Science and Technology, University of Macau, Macau 999078, China

ARTICLE INFO

Keywords:
Image completion
Low rank
Quaternion discrete cosine transform
Quaternion matrix
Sparsity
Truncated nuclear norm

ABSTRACT

This paper presents a novel approach for sparse regularization of low-rank quaternion matrix optimization problems. Quaternion matrices, which extend the concept of complex numbers to four dimensions, have shown promising applications in various fields. In this work, we exploit the inherent sparsity present in different signal types, such as audio formats and images, when represented in their respective bases. By introducing a sparse regularization term in the optimization objective. We propose a regularization technique that promotes sparsity in the Quaternion Discrete Cosine Transform (QDCT) domain for efficient and accurate solutions. By combining low-rank restriction with sparsity, the optimized model is updated using a two-step Alternating Direction Method of Multipliers (ADMM) algorithm. Experimental results on color images demonstrate the effectiveness of the proposed method, which outperforms existing relative methods. This superior performance underscores its potential for applications in computer vision and related fields.

1. Introduction

Color image completion aims to recover missing pixels using the limited known pixels in an image. Many matrix-based completion (MC) approaches have been designed for this purpose. Typically, a color image is processed by separating the red, green, and blue (RGB) channels into three matrices, and prior knowledge about the desired model is used for inpainting [1]. An effective and widely used prior knowledge is low-rankness. However, such MC approaches involve dimension reduction, which can destroy the structure of the color image. To avoid this, quaternion-based approaches have gradually become more commonly used in image processing, as these allow the values of one pixel in the color image to be put in three imaginary parts of one quaternion to form a more reliable quaternion matrix [2,3].

For color image completion in the quaternion domain, the typical prior knowledge is the low-rankness, analogous to the prior matrix-based cases. The authors in [4] proposed a low-rank quaternion approximation model based on modified quaternion nuclear norm (QNN). However, calculating these norms need to operate the computationally complex quaternion singular value decomposition (QSVD). To improve the time-consuming process, researchers in [5] developed low-rank quaternion matrix factorization approach by factorizing the target quaternion matrix into the product of two smaller quaternion factor matrices. Thus, the low-rank estimation process is more efficient because it only requires optimizing two smaller quaternion matrices. Still, similar to matrix-based cases, this factorization method may encounter difficulties in finding the global minimum and instead get stuck in local minima [6,7].

Based on low-rankness, the previously developed quaternion-based methods can thus process color images overall to obtain better recovery results; however, they ignore other important properties such as sparsity. The direct motivation to reconsider this can be derived from the fact that various kinds of signals, including audio and images, have naturally sparse structures, with regard to given bases such as Fourier and wavelet [8–10]. This fact has inspired new approaches in signal processing, and especially for vision tasks, such as face recognition [11,12], image recovery [13–16], and similar tasks. In terms of image completion, as highlighted in [17], sparsity is also an important property that can be used in MC.

In spite of the successes of these algorithms being encouraging, most of them are optimized only in the real domain. When images are optimized in the quaternion domain, the main direction is sparse representation (SR) [18,19], and, in terms of image completion, the results as seen in [20] are not very satisfactory. Hence, to develop more accu-

* Corresponding author.
E-mail addresses: liqiaoyoung@163.com (L. Yang), liuyang@zjnu.edu.cn (Y. Liu), kikou@umac.mo (K.I. Kou).

https://doi.org/10.1016/j.dsp.2024.104781

Available online 13 September 2024

rate reconstructions, sparsity as an additional information is considered in this paper to facilitate color image completion in the quaternion domain. This sparsity is depicted by QDCT, with low-rankness depicted using the quaternion truncated nuclear norm (QTNN). The novel model is named the Low-rank Quaternion Recovery with Sparse Regularization (LRQR-SR) model.

The main contributions of this work are as follows: This research focuses on quaternion MC by integrating low-rankness and sparsity. The key idea is that the quaternion-based method can maintain the structure of the color image, enabling sparsity to be expressed as an l_1 norm regularizer in the transformed domain. Additionally, a closed-form solution for the model, which combines the Frobenius norm and the l_1 norm, is proposed and backed by theoretical analysis. Extensive experimental results on real color images demonstrate the competitive performance of the proposed method compared to several state-of-the-art and comparable methods.

The remainder of this paper consists of four additional sections. Section 2 provides an overview of the relevant notations and basic knowledge about quaternions. In section 3, we introduce the model of low-rank quaternion recovery with sparse regularization. Section 5 compares the numerical experiment with other related methods. Finally, the conclusion is presented in Section 6.

2. Notations and preliminaries

2.1. Notations

In the real domain $\mathbb{R}$, we denote scalar, vector, and matrix as a, $\mathbf{a}$, and $\mathbf{A}$, respectively. In the quaternion domain $\mathbb{H}$, we denote scalar, vector, and matrix as $\dot{a}$, $\dot{\mathbf{a}}$, and $\dot{\mathbf{A}}$, respectively. Besides, we denote the complex space as $\mathbb{C}$. For a quaternion $\dot{q}$, we denote the real part and imaginary part as $\Re(\dot{q})$ and $\Im(\dot{q})$. We denote transpose, conjugate transpose, and inverse as $(\cdot)^T$, $(\cdot)^H$, and $(\cdot)^{-1}$, respectively. We use $\|\cdot\|_F$ and $\|\cdot\|_*$ to represent the Frobenius norm and nuclear norm. We define the inner product of $*_1$ and $*_2$ as $\langle *_1 \cdot *_2 \rangle \triangleq \mathrm{tr}(*_1^H *_2)$, where $tr(\cdot)$ is the trace function. Both $\mathbf{I}_{r\times r}$ and $\mathbf{I}_r$ denote the $r \times r$ identity matrix.

2.2. Preliminaries

Quaternions are proposed by Hamilton in 1843 [21]. A quaternion number $\dot{q} \in \mathbb{H}$ is combined by a real part and three imagery parts, and can be written as following form:

$$\dot{q} = q_0 + q_1 i + q_2 j + q_3 k, \tag{1}$$

where $q_n \in \mathbb{R}$ $(n = 0, 1, 2, 3)$, and i, j, k are three imaginary number units which have the following relationships:

$$i^2 = j^2 = k^2 = ijk = -1, ij = -ji = k, jk = -kj = i, ki = -ik = j. \tag{2}$$

$\Re(\dot{q}) \triangleq q_0$ is the real part of $\dot{q}$. $\Im(\dot{q}) \triangleq q_1 i + q_2 j + q_3 k$ is the imaginary part of $\dot{q}$. Hence $\dot{q} = \Re(\dot{q}) + \Im(\dot{q})$. Besides, when real part $q_0 = 0$, $\dot{q}$ is a pure quaternion. The conjugate and the modulus of $\dot{q}$ are defined as: $\dot{q}^* \triangleq q_0 - q_1 i - q_2 j - q_3 k$ and $|\dot{q}| \triangleq \sqrt{\dot{q}\dot{q}^*} = \sqrt{q_0^2 + q_1^2 + q_2^2 + q_3^2}$. It is important to note that the multiplication in the quaternion domain is not commutative $\dot{p}\dot{q} \neq \dot{p}\dot{q}$.

For quaternion matrix $\dot{\mathbf{Q}} = (\dot{q}_{ij}) \in \mathbb{H}^{M\times N}$, where $\dot{\mathbf{Q}} = \mathbf{Q}_0 + \mathbf{Q}_1 i + \mathbf{Q}_2 j + \mathbf{Q}_3 k$ and $\mathbf{Q}_n \in \mathbb{R}^{M\times N}$ $(n = 0, 1, 2, 3)$ are real matrices. When $\mathbf{Q}_0 = \mathbf{0}$, $\dot{\mathbf{Q}}$ is a pure quaternion matrix. The Frobenius norm is defined as: $\|\dot{\mathbf{Q}}\|_F = \sqrt{\sum_{i=1}^{M}\sum_{j=1}^{N} |\dot{q}_{ij}|^2} = \sqrt{tr(\dot{\mathbf{Q}}^H \dot{\mathbf{Q}})}$.

Definition 1 *(The Cayley-Dickson form [22]).* The Cayley-Dickson form of quaternion matrix $\dot{\mathbf{Q}} = \mathbf{Q}_0 + \mathbf{Q}_1 i + \mathbf{Q}_2 j + \mathbf{Q}_3 k \in \mathbb{H}^{M\times N}$ is $\dot{\mathbf{Q}} = \mathbf{Q}_p + \mathbf{Q}_q j$, where $\mathbf{Q}_p = \mathbf{Q}_0 + \mathbf{Q}_1 i$ and $\mathbf{Q}_q = \mathbf{Q}_2 + \mathbf{Q}_3 i \in \mathbb{C}^{M\times N}$. Then the isomorphic complex matrix representation of quaternion matrix $\dot{\mathbf{Q}}$ can be denoted as $\mathbf{Q}_c \in \mathbb{C}^{2M\times 2N}$:

$$\mathbf{Q}_c = \begin{pmatrix} \mathbf{Q}_p & \mathbf{Q}_q \\ -\mathbf{Q}_q^* & \mathbf{Q}_p^* \end{pmatrix}_{2M\times 2N}.$$

Definition 2 *(The rank of quaternion matrix [23]).* The rank of quaternion matrix $\dot{\mathbf{Q}} = (\dot{q}_{ij}) \in \mathbb{H}^{M\times N}$ is defined as the maximum number of right (left) linearly independent columns (rows) of $\dot{\mathbf{Q}}$.

Theorem 1 *(QSVD [23]). Given a quaternion matrix $\dot{\mathbf{Q}} \in \mathbb{H}^{M\times N}$ be of rank r. There are two unitary quaternion matrices $\dot{\mathbf{U}} \in \mathbb{H}^{M\times M}$ and $\dot{\mathbf{V}} \in \mathbb{H}^{N\times N}$ such that*

$$\dot{\mathbf{Q}} = \dot{\mathbf{U}} \begin{pmatrix} \mathbf{\Sigma}_r & \mathbf{0} \\ \mathbf{0} & \mathbf{0} \end{pmatrix} \dot{\mathbf{V}}^H = \dot{\mathbf{U}} \mathbf{\Lambda} \dot{\mathbf{V}}^H, \tag{3}$$

where $\mathbf{\Sigma}_r = diag(\sigma_1, \cdots, \sigma_r) \in \mathbb{R}^{r\times r}$, and all singular values $\sigma_i > 0, i = 1, \cdots, r$.

Definition 3 *(QNN [4,24]).* The nuclear norm of the quaternion matrix $\dot{\mathbf{Q}} \in \mathbb{H}^{M\times N}$ is defined as $\|\dot{\mathbf{Q}}\|_* = \sum_{i=1}^{\min(M,N)} \sigma_i(\dot{\mathbf{Q}})$, where σ_i is singular value that can be obtained from the QSVD of $\dot{\mathbf{Q}}$.

As observed in [25], the bigger singular values would maintain more information on the color image than smaller singular values. Moreover, the first few largest singular values do not change the rank. Hence, the quaternion-based truncated nuclear norm (QTNN) is developed as follows.

Definition 4 *(QTNN [26]).* The sum of $\min(M, N) - r$ minimum singular values is the quaternion truncated nuclear norm of the quaternion matrix $\dot{\mathbf{Q}} \in \mathbb{H}^{M\times N}$, i.e., $\|\dot{\mathbf{Q}}\|_r = \sum_{i=r+1}^{\min(M,N)} \sigma_i(\dot{\mathbf{Q}})$.

Theorem 2 *([26]). For any quaternion matrix $\dot{\mathbf{Q}} \in \mathbb{H}^{M\times N}$, and any matrices $\dot{\mathbf{A}} \in \mathbb{H}^{r\times M}$ and $\dot{\mathbf{B}} \in \mathbb{H}^{r\times N}$ that are satisfied with $\dot{\mathbf{A}}\dot{\mathbf{A}}^H = \mathbf{I}_{r\times r}$ and $\dot{\mathbf{B}}\dot{\mathbf{B}}^H = \mathbf{I}_{r\times r}$. r is any positive integer $(r \leq \min(M, N))$, we have*

$$|\, tr(\dot{\mathbf{A}}\dot{\mathbf{Q}}\dot{\mathbf{B}}^H) \,| \leq \sum_{i=1}^{r} \sigma_i(\dot{\mathbf{Q}}). \tag{4}$$

Besides, $\max|tr(\dot{\mathbf{A}}\dot{\mathbf{Q}}\dot{\mathbf{B}}^H)| = \sum_{i=1}^{r} \sigma_i(\dot{\mathbf{Q}})$.

3. Low-rank quaternion recovery with sparse regularization

3.1. Problem formulation

Let $\dot{\mathbf{O}} \in \mathbb{H}^{M\times N}$ be the partial observed color image. The purpose is to recover $\dot{\mathbf{X}} \in \mathbb{H}^{M\times N}$ by improving QNN as the characterization of the low-rank property more accurately. The QNN model can be formulated as

$$\min_{\dot{\mathbf{X}}} \|\dot{\mathbf{X}}\|_* \qquad \text{s.t.} \quad P_\Omega(\dot{\mathbf{X}}) = P_\Omega(\dot{\mathbf{O}}), \tag{5}$$

where Ω is the index set of the observed data, and the linear operation $P_\Omega(*)$ is the operator that indicates that the elements in Ω are remain while other elements are zero.

While being low rank is a feasible condition for MC, it is often insufficient on its own [17]. Building upon this observation and the successful utilization of sparsity in MC [27,14,28], this paper introduces the LRQR-SR model. The LRQR-SR model incorporates both a low-rank constraint and sparsity in the quaternion domain. Specifically, the low-rank constraint is represented using QTNN, while sparsity is achieved through the use of the l_1 norm. By simultaneously considering both low-rank and sparsity, the LRQR-SR model enhances the effectiveness of quaternion-based matrix completion tasks.

As the several largest singular values will not influence the rank, the QTNN model is proposed, and the estimation of low-rankness should thus be more accurate. Based on model (5) and Definition 4, this model is formulated as

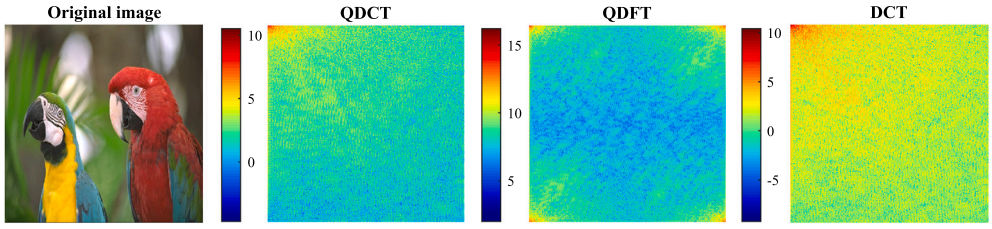

Fig. 1. The comparison of energy accumulation under different transformations.

$$\min_{\dot{\mathbf{X}}} \| \dot{\mathbf{X}} \|_r \quad \text{s.t.} \quad P_\Omega(\dot{\mathbf{X}} - \dot{\mathbf{O}}) = 0, \tag{6}$$

where $\|\dot{\mathbf{X}}\|_r = \sum_{i=r+1}^{\min(m,n)} \sigma_i(\dot{\mathbf{X}}) = \sum_{i=1}^{\min(m,n)} \sigma_i(\dot{\mathbf{X}}) - \sum_{i=r}^{\min(m,n)} \sigma_i(\dot{\mathbf{X}}) = \| \dot{\mathbf{X}} \|_* - \sum_{i=r}^{\min(m,n)} \sigma_i(\dot{\mathbf{X}})$.

As in the previously mentioned strategies, the quaternion matrix is assumed to be sparse in a certain transformed domain. Hence, the resulting model can be formulated as

$$\min_{\dot{\mathbf{X}}} \| \dot{\mathbf{X}} \|_* - \sum_{i=r}^{\min(m,n)} \sigma_i(\dot{\mathbf{X}}) + \lambda \| \dot{\mathbf{D}} \|_1 \quad \text{s.t.} \quad P_\Omega(\dot{\mathbf{X}} - \dot{\mathbf{O}}) = 0, \mathcal{T}(\dot{\mathbf{X}}) = \dot{\mathbf{D}}, \tag{7}$$

where $\mathcal{T}(\cdot)$ is the transform operator, $\dot{\mathbf{D}}$ is the transformed quaternion matrix, and λ is a positive number.

However, it is hard to solve problem (7) directly due to the fact that QTNN is nonconvex. To address this problem, Theorem 2 is applied such that problem (7) can be rewritten as

$$\begin{aligned} &\min_{\dot{\mathbf{X}}} \| \dot{\mathbf{X}} \|_* - \max_{\dot{\mathbf{A}}\dot{\mathbf{A}}^H = \mathbf{I}, \dot{\mathbf{B}}\dot{\mathbf{B}}^H = \mathbf{I}} |tr(\dot{\mathbf{A}}\dot{\mathbf{X}}\dot{\mathbf{B}}^H)| + \lambda \| \dot{\mathbf{D}} \|_1 \\ &\text{s.t.} \quad P_\Omega(\dot{\mathbf{X}} - \dot{\mathbf{O}}) = 0 \qquad \mathcal{T}(\dot{\mathbf{X}}) = \dot{\mathbf{D}}, \end{aligned} \tag{8}$$

where $\dot{\mathbf{A}} = (\dot{\mathbf{u}}_1, \cdots \dot{\mathbf{u}}_r)^H$ and $\dot{\mathbf{B}} = (\dot{\mathbf{v}}_1, \cdots \dot{\mathbf{v}}_r)^H$. $\{\dot{\mathbf{u}}_1, \cdots \dot{\mathbf{u}}_r\}$ and $\{\dot{\mathbf{v}}_1, \cdots \dot{\mathbf{v}}_r\}$ are the first r columns of $\dot{\mathbf{U}}$ and $\dot{\mathbf{V}}$. $\dot{\mathbf{U}}$ and $\dot{\mathbf{V}}$ are left and right unitary quaternion matrices that are calculated by QSVD of $\dot{\mathbf{X}}$.

In this way, the whole procedure of the method can be divided into two main steps: in the first step, the quaternion matrices are computed by QSVD, and then the main goal becomes to optimize problem (8). The overall procedure is summarized in Algorithm 1.

Algorithm 1 Low-rank Quaternion Recovery with Sparse Regularization.

Input: the observed quaternion matrix $\dot{\mathbf{O}} \in \mathbb{H}^{M \times N}$, the position set of observed elements Ω, and the tolerance ϵ_0.

1: **Initial** the initial number of iteration $k = 1$, $\dot{\mathbf{X}}_1 = \dot{\mathbf{O}}$.
2: **Repeat**
3: **Step 1.** Calculating the QSVD of the given $\dot{\mathbf{X}}_k$
$[\dot{\mathbf{U}}_k, \mathbf{\Sigma}_k, \dot{\mathbf{V}}_k] = \text{QSVD}(\dot{\mathbf{X}}_k)$
4: where $\dot{\mathbf{U}}_k = (\dot{\mathbf{u}}_1, \cdots, \dot{\mathbf{u}}_m) \in \mathbb{H}^{M \times M}$,
$\dot{\mathbf{V}}_k = (\dot{\mathbf{v}}_1, \cdots, \dot{\mathbf{v}}_n) \in \mathbb{H}^{N \times N}$.
5: Calculating $\dot{\mathbf{A}}_k = (\dot{\mathbf{u}}_1, \cdots, \dot{\mathbf{u}}_r)^T \in \mathbb{H}^{r \times M}$ and
$\dot{\mathbf{B}}_k = (\dot{\mathbf{v}}_1, \cdots, \dot{\mathbf{v}}_r)^T \in \mathbb{H}^{r \times N}$.
6: **Step 2.** Solving the optimization problem as followed
$\dot{\mathbf{X}}_{k+1} = \arg\min_{\dot{\mathbf{X}}} \| \dot{\mathbf{X}} \|_* - |tr(\dot{\mathbf{A}}_k \dot{\mathbf{X}} \dot{\mathbf{B}}_k^H)| + \lambda \| \dot{\mathbf{D}} \|_1,$
s.t. $P_\Omega(\dot{\mathbf{X}} - \dot{\mathbf{O}}) = 0 \qquad \mathcal{T}(\dot{\mathbf{X}}) = \dot{\mathbf{D}}.$
7: **Until convergence** $\|\dot{\mathbf{X}}_{k+1} - \dot{\mathbf{X}}_k\|_F \le \epsilon_0$, $\dot{\mathbf{X}}_{opt} = \dot{\mathbf{X}}_{k+1}$.

Output: the recovered quaternion matrix $\dot{\mathbf{X}}_{opt}$.

3.2. Quaternion discrete cosine transform

3.2.1. The reasons for utilizing QDCT

Operating in the quaternion domain for image recovery offers several advantages. By representing color images using quaternion algebra, the RGB structure of the image can be preserved, leading to more accurate and reliable image recovery results. In addition, the spectral coefficients obtained using QDCT have strong energy and good redundancy elimination characteristics [29], while QDCT itself is easy to quantitatively analyze. Finally, in the real and complex fields, the energy concentration of the input information throughout two-dimensional DCT is higher than that of the input information after discrete Fourier transform (DFT). Research into QDCT is driven by the existence of successful applications in both the real and complex domains, and for these reasons, QDCT is adopted in the proposed method.

Fig. 1 gives an illustration of the proposed sparse representation on the color image "*Parrot*". The first image is the original image; the second, third, and fourth image respectively display the coefficients after QDCT, quaternion DFT (QDFT), and DCT (for grayscale image) using a logarithmic scale. After transformation, the coefficients of QDCT and DCT are mainly concentrated in the upper left corner, and most of the remaining coefficients are close to zero. However, after QDFT transformation, the coefficients are mainly concentrated at four corners, which means that utilizing cosine transform is superior to Fourier transform for depicting the sparsity of color images in the quaternion domain. Besides, when comparing QDCT with DCT, especially in the upper left corner, it can be observed that QDCT has higher energy compaction than DCT.

3.2.2. Definition of QDCT

As the multiplication of quaternions is non-commutative, there are two forms of QDCT: a left-handed form QDCT_L and a right-handed form QDCT_R. These can be formulated as the following equations, respectively [30]:

$$\text{QDCT}_L(p,s) = \alpha(p)\alpha(s) \sum_{m=0}^{M-1} \sum_{n=0}^{N-1} \dot{u} \cdot \dot{\mathbf{F}}(m,n) \cdot C(p,s,m,n) \tag{9}$$

$$\text{QDCT}_R(p,s) = \alpha(p)\alpha(s) \sum_{m=0}^{M-1} \sum_{n=0}^{N-1} \dot{\mathbf{F}}(m,n) \cdot C(p,s,m,n) \cdot \dot{u}, \tag{10}$$

where $\dot{\mathbf{F}}(m,n) \in \mathbb{H}^{M \times N}$, m and n is the row and column of quaternion matrix $\dot{\mathbf{F}}$. $\dot{u}$ is a pure quaternion and satisfies $\dot{u}^2 = -1$. The values of $\alpha(p), \alpha(s)$ and $C(p,s,m,n)$ are analogous to DCT in the real domain:

$$\alpha(p) = \begin{cases} \sqrt{1/M} & p = 0 \\ \sqrt{2/M} & p \neq 0, \end{cases} \quad \alpha(s) = \begin{cases} \sqrt{1/N} & s = 0 \\ \sqrt{2/N} & s \neq 0. \end{cases} \tag{11}$$

$$C(p,s,m,n) = \cos[\frac{\pi(2m+1)p}{2M}] \cos[\frac{\pi(2n+1)p}{2N}]. \tag{12}$$

Besides, the corresponding inverse transformation of QDCT is the Inverse Quaternion Discrete Cosine Transform (IQDCT). These are thus the transformation pairs of each other, and satisfy the following relationship:

$$\begin{aligned} \dot{\mathbf{F}}(m,n) &= \text{IQDCT}_L[\text{QDCT}_L(\dot{\mathbf{F}}(m,n))], \\ \dot{\mathbf{F}}(m,n) &= \text{IQDCT}_R[\text{QDCT}_R(\dot{\mathbf{F}}(m,n))]. \end{aligned} \tag{13}$$

In the proposed algorithm, QDCT_L is utilized to calculate QDCT.

3.2.3. Calculation of QDCT$_L$

To simplify the calculation of QDCT, we take full advantage of the Cayley Dickson form seen in Definition 1, as in [30] is used. The whole process of QDCT$_L$ calculation is as follows:

a Transforming the given quaternion matrix $\dot{\mathbf{F}}(m,n) \in \mathbb{H}^{M\times N}$ to the Cayley Dickson form

$$\dot{\mathbf{F}}(m,n) = \mathbf{F}_p(m,n) + \mathbf{F}_q(m,n)j, \tag{14}$$

where $\mathbf{F}_p(m,n)$ and $\mathbf{F}_q(m,n) \in \mathbb{C}^{M\times N}$.

b Calculating the DCT of complex matrices $\mathbf{F}_p(m,n)$ and $\mathbf{F}_q(m,n)$. The results are denoted as $\mathrm{DCT}_C(\mathbf{F}_p(m,n))$ and $\mathrm{DCT}_C(\mathbf{F}_q(m,n))$, respectively.

c Using $\mathrm{DCT}_C(\mathbf{F}_p(m,n))$ and $\mathrm{DCT}_C(\mathbf{F}_q(m,n))$ to form a quaternion matrix

$$\dot{\mathbf{F}}'(m,n) = \mathrm{DCT}_C(\mathbf{F}_p(m,n)) + \mathrm{DCT}_C(\mathbf{F}_q(m,n))j. \tag{15}$$

d Multiplying $\dot{\mathbf{F}}'(m,n)$ with the quaternion factor $\dot{u}$ to get the final result QDCT$_L$

$$\mathrm{QDCT}_L(\dot{\mathbf{F}}(m,n)) = \dot{u}\cdot\dot{\mathbf{F}}'(m,n). \tag{16}$$

3.3. ADMM-based optimization algorithm

Following the model we discussed in subsection 3.1 and the transformation introduced in subsection 3.2, ADMM was adopted to optimize problem (8). This involves introducing auxiliary variable $\dot{\mathbf{H}}$ and reformulating (8) as

$$\begin{aligned} &\min_{\dot{\mathbf{X}}} \| \dot{\mathbf{X}} \|_* - \max_{\dot{\mathbf{A}}\dot{\mathbf{A}}^H=\mathbf{I},\dot{\mathbf{B}}\dot{\mathbf{B}}^H=\mathbf{I}} |tr(\dot{\mathbf{A}}\dot{\mathbf{H}}\dot{\mathbf{B}}^H)| + \lambda \| \dot{\mathbf{D}} \|_1 \\ &\text{s.t.} \quad P_\Omega(\dot{\mathbf{X}} - \dot{\mathbf{O}}) = 0 \qquad \dot{\mathbf{H}} = \dot{\mathbf{X}} \qquad \mathcal{T}_{QDCT_L}(\dot{\mathbf{X}}) = \dot{\mathbf{D}}. \end{aligned} \tag{17}$$

In analogy with the ADMM framework adopted in the complex domain [31], as the multiplication is not commutative in the quaternion domain, the augmented Lagrangian function of (17) can be written as

$$\begin{aligned} L(\dot{\mathbf{X}},\dot{\mathbf{H}},\dot{\mathbf{D}},\dot{\mathbf{Y}},\dot{\mathbf{Z}},\beta) =& \| \dot{\mathbf{X}} \|_* - |tr(\dot{\mathbf{A}}\dot{\mathbf{H}}\dot{\mathbf{B}}^H)| + \lambda \| \dot{\mathbf{D}} \|_1 + \Re(tr(\dot{\mathbf{Y}}^H(\dot{\mathbf{X}} - \dot{\mathbf{H}}))) \\ &+ \frac{\beta}{2} \| \dot{\mathbf{X}} - \dot{\mathbf{H}} \|_F^2 + \Re(tr(\dot{\mathbf{Z}}^H(\dot{\mathbf{D}} - \mathcal{T}_{QDCT_L}(\dot{\mathbf{X}})))) + \frac{\beta}{2} \| \dot{\mathbf{D}} - \mathcal{T}_{QDCT_L}(\dot{\mathbf{X}}) \|_F^2, \end{aligned} \tag{18}$$

where $\dot{\mathbf{Y}}$ and $\dot{\mathbf{Z}}$ are the Lagrange multipliers, and β is the positive penalty parameter. The $\dot{\mathbf{X}}$ subproblem is

$$\begin{aligned} \dot{\mathbf{X}}^{p+1} &= \arg\min_{\dot{\mathbf{X}}} \| \dot{\mathbf{X}} \|_* + \Re(tr(\dot{\mathbf{Y}}^{pH}(\dot{\mathbf{X}} - \dot{\mathbf{H}}^p))) + \frac{\beta^p}{2} \| \dot{\mathbf{X}} - \dot{\mathbf{H}}^p \|_F^2 \\ &\quad + \Re(tr(\dot{\mathbf{Z}}^{pH}(\dot{\mathbf{D}}^p - \mathcal{T}_{QDCT_L}(\dot{\mathbf{X}})))) + \frac{\beta^p}{2} \| \dot{\mathbf{D}}^p - \mathcal{T}_{QDCT_L}(\dot{\mathbf{X}}) \|_F^2 \\ &= \arg\min_{\dot{\mathbf{X}}} \| \dot{\mathbf{X}} \|_* + \frac{\beta^p}{2} \| \dot{\mathbf{X}} - \dot{\mathbf{H}}^p + \dot{\mathbf{Y}}^p/\beta^p \|_F^2 \\ &\quad + \frac{\beta^p}{2} \| \dot{\mathbf{D}}^p - \mathcal{T}_{QDCT_L}(\dot{\mathbf{X}}) + \dot{\mathbf{Z}}^p/\beta^p \|_F^2 . \end{aligned} \tag{19}$$

In the last term of (19), $\dot{\mathbf{X}}$ can not be separated directly as the transformation. Despite this, the Parseval theorem in the quaternion domain indicates that the total energy of signal computed in the quaternion domain and total energy of signal computed in the spatial domain are the same [32,33]. This means that a unitary transformation preserves energy conservation under the Frobenius norm, and thus the last term of (19) can be rewritten as

$$\frac{\beta^p}{2} \| \dot{\mathbf{D}}^p - \mathcal{T}_{QDCT_L}(\dot{\mathbf{X}}) + \dot{\mathbf{Z}}^p/\beta^p \|_F^2 = \frac{\beta^p}{2} \| \mathcal{T}_{IQDCT_L}(\dot{\mathbf{D}}^p + \dot{\mathbf{Z}}^p/\beta^p) - \dot{\mathbf{X}} \|_F^2, \tag{20}$$

where the $\mathcal{T}_{IQDCT_L}$ is the inverse transformation of QDCT$_L$. For a more concise representation, let $\mathcal{T}$ denote $\mathcal{T}_{QDCT_L}$ and $\mathcal{IT}$ denote $\mathcal{T}_{IQDCT_L}$. Consequently, (19) can be reformulated as

$$\begin{aligned} \dot{\mathbf{X}}^{p+1} &= \arg\min_{\dot{\mathbf{X}}} \| \dot{\mathbf{X}} \|_* + \frac{\beta_k}{2} \| \dot{\mathbf{X}} - \dot{\mathbf{H}}^p + \dot{\mathbf{Y}}^p/\beta^p \|_F^2 \\ &\quad + \frac{\beta^p}{2} \| \mathcal{IT}(\dot{\mathbf{D}}^p + \dot{\mathbf{Z}}^p/\beta^p) - \dot{\mathbf{X}} \|_F^2 \\ &= \arg\min_{\dot{\mathbf{X}}} \| \dot{\mathbf{X}} \|_* + \beta^p \| \dot{\mathbf{X}} - \frac{1}{2}[\dot{\mathbf{H}}^p + \dot{\mathbf{Y}}^p/\beta^p + \mathcal{IT}(\dot{\mathbf{D}}^p + \dot{\mathbf{Z}}^p/\beta^p)] \|_F^2 . \end{aligned} \tag{21}$$

The closed solution of the above problem is

$$\dot{\mathbf{X}}^{p+1} = \mathfrak{D}_{\frac{1}{2\beta^p}}(\frac{1}{2}[\dot{\mathbf{H}}^p + \dot{\mathbf{Y}}^p/\beta^p + \mathcal{IT}(\dot{\mathbf{D}}^p + \dot{\mathbf{Z}}^p/\beta^p)]), \tag{22}$$

where $\mathfrak{D}_\tau(*)$ is the quaternion singular value shrinkage operator [4] is defined as

$$\mathfrak{D}_\tau(\dot{\mathbf{A}}) = \dot{\mathbf{U}}\mathfrak{D}_\tau(\mathbf{\Sigma})\dot{\mathbf{V}}^H, \quad \mathfrak{D}_\tau(\mathbf{\Sigma}) = diag(\max\{\sigma_i - \tau, 0\}), \tag{23}$$

where $\dot{\mathbf{U}}$, $\dot{\mathbf{V}}$, and σ_i are obtained by computing QSVD of quaternion matrix $\dot{\mathbf{A}} = \dot{\mathbf{U}}\mathbf{\Sigma}\dot{\mathbf{V}}^H, \mathbf{\Sigma} = diag(\sigma_1,\cdots,\sigma_r,0\cdots,0) \in \mathbb{R}^{M\times N}$.

The $\dot{\mathbf{D}}$ subproblem is

$$\begin{aligned} \dot{\mathbf{D}}^{p+1} &= \arg\min_{\dot{\mathbf{D}}} \lambda \| \dot{\mathbf{D}} \|_1 + \Re(tr(\dot{\mathbf{Z}}^{pH}(\dot{\mathbf{D}} - \mathcal{T}(\dot{\mathbf{X}}^{p+1})))) \\ &\quad + \frac{\beta^p}{2} \| \dot{\mathbf{D}} - \mathcal{T}(\dot{\mathbf{X}}^{p+1}) \|_F^2 \\ &= \arg\min_{\dot{\mathbf{D}}} \lambda \| \dot{\mathbf{D}} \|_1 + \frac{\beta^p}{2} \| \dot{\mathbf{D}} - \mathcal{T}(\dot{\mathbf{X}}^{p+1}) + \dot{\mathbf{Z}}^{pH}/\beta^p \|_F^2 . \end{aligned} \tag{24}$$

To obtain the optimal solution of (24), we have the following theorem.

Theorem 3. *For any $\lambda > 0$, the closed solution of problem $\min_{\dot{\mathbf{X}}} \lambda \| \dot{\mathbf{X}} \|_1 + \| \dot{\mathbf{Y}} - \dot{\mathbf{X}} \|_F^2$ can be given by*

$$\dot{\mathbf{X}}_{opt} = \mathcal{S}_{2\lambda}(\dot{\mathbf{Y}}), \tag{25}$$

where $\mathcal{S}_\tau(\cdot)$ represents the element-wise soft thresholding operator defined by

$$\mathcal{S}_\tau(\dot{\mathbf{x}}) = \frac{\dot{\mathbf{x}}}{|\dot{\mathbf{x}}|} max\{|\dot{\mathbf{x}}| - \tau, 0\}. \tag{26}$$

4. Proof of Theorem 3

According to [4], we need to prove

$$\min_{\dot{\mathbf{X}}} \| \dot{\mathbf{Y}} - \dot{\mathbf{X}} \|_F^2 + \lambda \| \dot{\mathbf{X}} \|_1 \tag{27}$$

has one unique optimal solution $\dot{\mathbf{X}}_\star$ and $\dot{\mathbf{X}}_\star$ equals to $\dot{\mathbf{X}}_{opt}$ defined in (25).

Proof. It can be observed that two terms in (27) are convex, hence, (27) has one unique optimal solution. Based on the rules of quaternion matrix derivatives in [34], $\dot{\mathbf{X}}_\star$ must satisfy the following formula:

$$\dot{0} \in \dot{\mathbf{X}}_\star - \dot{\mathbf{Y}} + 2\lambda\partial \| \dot{\mathbf{X}}_\star \|_1, \tag{28}$$

where $\partial \| \dot{\mathbf{X}}_\star \|_1$ represents the subgradient of $\| \dot{\mathbf{X}}_\star \|_1$. Following [20], the subgradient of the l_1 norm at $\dot{\mathbf{X}}_\star$ is given by

$$\partial \| \dot{\mathbf{X}}_\star \|_1 = \{\dot{\mathbf{G}} \in \mathbb{H}^{M\times N} : \dot{\mathbf{G}} = direc(\dot{\mathbf{X}}_\star) + \dot{\mathbf{F}}, P_\Omega(\dot{\mathbf{F}}) = 0, \| \dot{\mathbf{F}} \|_\infty \le 1\}, \tag{29}$$

where $direc(\dot{\mathbf{X}}_\star)$ is a $M \times N$ matrix with the entries computed by $[\frac{x_{ij}}{|x_{ij}|}]_{M\times N}$. Then, $\dot{\mathbf{X}}_{opt}$ need to be proved to satisfy (28).

When $\dot{y} > 2\lambda$, $\dot{x} > 0$, then

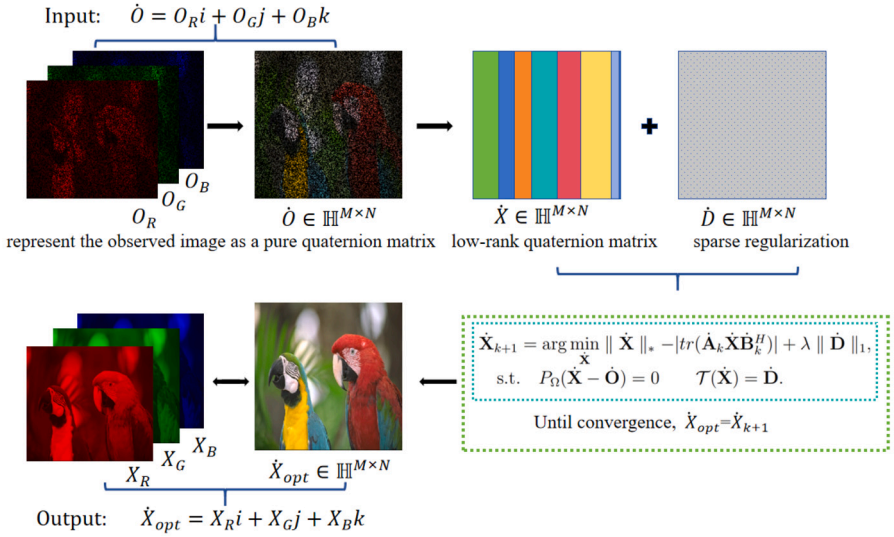

Fig. 2. The flowchart of color image recovery using LRQR-SR.

Fig. 3. The eight color images, each with a size of $256 \times 256 \times 3$, are named *Tree*, *Beans*, *Flower*, *Vegetable*, *House*, *Airplane*, *Barbara*, and *Splash*, respectively.

$\dot{y} - \dot{x} = \dot{y} - \frac{\dot{y}}{|\dot{y}|}\max\{|\dot{y}| - 2\lambda, 0\} = \dot{y} - (\dot{y} - 2\lambda) = 2\lambda$. Then, $\dot{x}_{opt} - \dot{y} + 2\lambda\partial \| \dot{x}_{opt} \|_1 = -2\lambda + 2\lambda = 0$.
When $-2\lambda \leqslant \dot{y} \leqslant 2\lambda$, $\dot{x} = 0$, then
$\dot{y} - \dot{x} = \dot{y}$. Let $\dot{\mathbf{F}} = \frac{1}{2\lambda}\dot{\mathbf{Y}}$, we have $\| \dot{\mathbf{F}} \|_\infty \leqslant 1$. Then, $\dot{x}_{opt} - \dot{y} + 2\lambda\partial \| \dot{x}_{opt} \|_1 = -\dot{y} + \dot{y} = 0$.
When $\dot{y} < -2\lambda$, $\dot{x} < 0$, then
$\dot{y} - \dot{x} = \dot{y} + (-\dot{y} - 2\lambda) = -2\lambda = 2\lambda(-1)$. Then, $\dot{x}_{opt} - \dot{y} + 2\lambda\partial \| \dot{x}_{opt} \|_1 = 2\lambda - 2\lambda = 0$.
Based on the above discussions, we can obtain that $\dot{0} \in \dot{\mathbf{X}}_{opt} - \dot{\mathbf{Y}} + 2\lambda\partial \| \dot{\mathbf{X}}_{opt} \|_1$, which means that $\dot{\mathbf{X}}_{opt} = \dot{\mathbf{X}}_\star$. □

The proof of Theorem 3 is given in the Appendix. Based on Theorem 3, problem (24) has a closed-form solution given by

$$\dot{\mathbf{D}}^{p+1} = \mathcal{S}_{\frac{4\lambda}{\beta^p}}(\mathcal{T}(\dot{\mathbf{X}}^{p+1}) - \dot{\mathbf{Z}}^{pH}/\beta^p). \tag{30}$$

The $\dot{\mathbf{H}}$ subproblem is

$$\begin{aligned}\dot{\mathbf{H}}^{p+1} &= \arg\min_{\dot{\mathbf{H}}} -|tr(\dot{\mathbf{A}}\dot{\mathbf{H}}\dot{\mathbf{B}}^H)| + \Re(tr(\dot{\mathbf{Y}}^{pH}(\dot{\mathbf{X}}^{p+1} - \dot{\mathbf{H}}))) \\ &\quad + \frac{\beta^p}{2} \| \dot{\mathbf{X}}^{p+1} - \dot{\mathbf{H}} \|_F^2 \\ &= \arg\min_{\dot{\mathbf{H}}} \frac{\beta^p}{2} \| \dot{\mathbf{X}}^{p+1} - \dot{\mathbf{H}} + \dot{\mathbf{Y}}^p/\beta^p + \dot{\mathbf{A}}^H\dot{\mathbf{B}}/\beta^p \|_F^2 .\end{aligned} \tag{31}$$

Following equation (31), we can obtain

$$\dot{\mathbf{H}}^{p+1} = \dot{\mathbf{X}}^{p+1} + \dot{\mathbf{Y}}^p/\beta^p + \dot{\mathbf{A}}^H\dot{\mathbf{B}}/\beta^p. \tag{32}$$

Moreover, the observed data should remain unchanged in each iteration such that

$$\dot{\mathbf{H}}^{p+1} = P_{\Omega^C}(\dot{\mathbf{H}}^{p+1}) + P_\Omega(\dot{\mathbf{O}}). \tag{33}$$

The update of penalty parameter β^p is

$$\beta^{p+1} = \min\{\rho\beta^p, \beta_{\max}\}, \tag{34}$$

where $\beta_{\max}$ is the given maximum value of the penalty parameter, and $\rho \geq 1$ is a constant parameter. Because the convergence speed of the ADMM algorithm can be affected by the choice of the penalty parameter β^{p+1}. When it is set to a small value, the algorithm tends to converge slowly due to the updates are conservative. Conversely, if it is set to a large value, the algorithm may become unstable or diverge altogether. So we adopted a dynamically changing β^{p+1}, and obtained the initial value through careful tuning.

Model (17) is the problem in Step 2 listed in Algorithm 1, so that the whole procedure to solve it is summarized in Algorithm 2. Fig. 2 represents the flowchart of the proposed LRQR-SR.

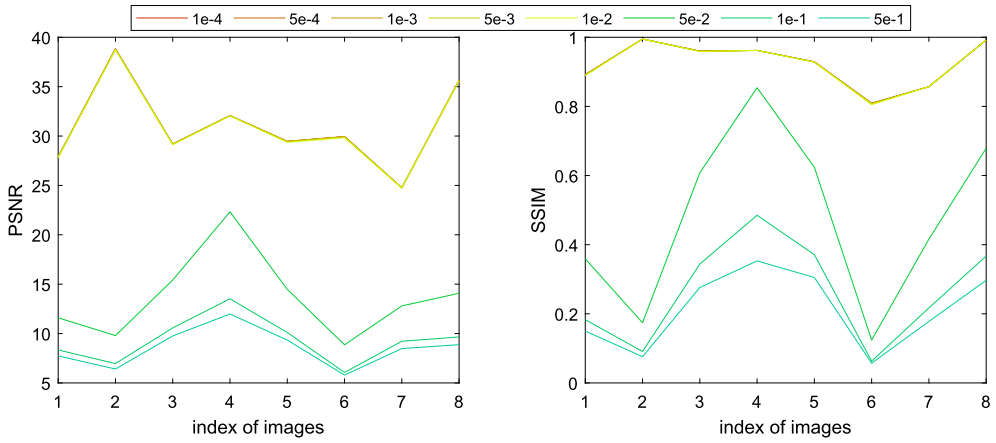

Fig. 4. The PSNR and SSIM values obtained by the proposed LRQR-SR algorithm using different β^1 with other parameters fixed and SR = 0.5.

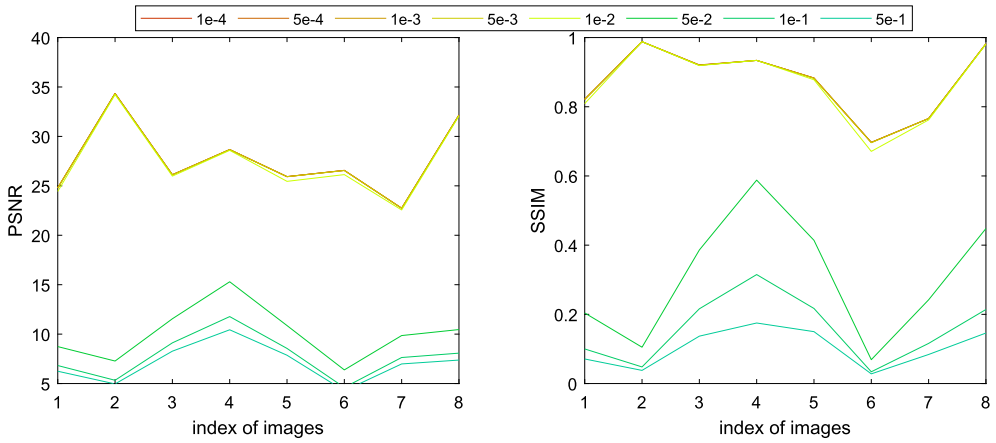

Fig. 5. The PSNR and SSIM values obtained by the proposed LRQR-SR algorithm using different β^1 with other parameters fixed and SR = 0.3.

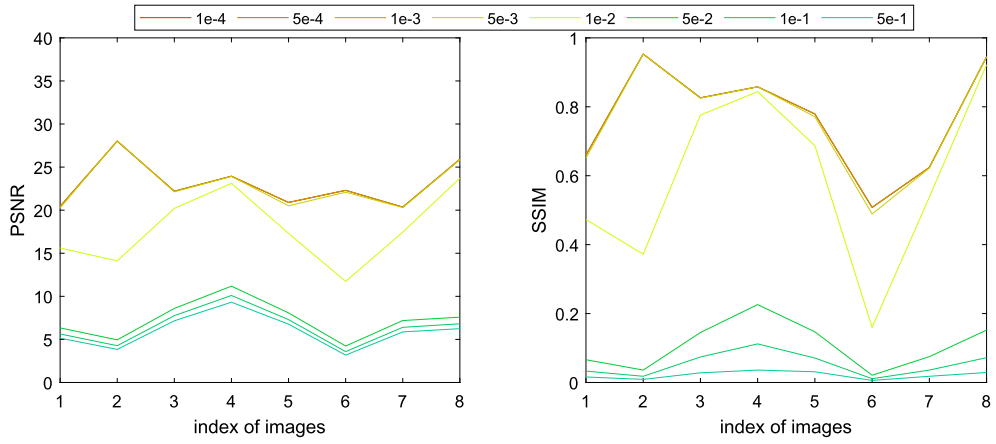

Fig. 6. The PSNR and SSIM values obtained by the proposed LRQR-SR algorithm using different β^1 with other parameters fixed and SR = 0.1.

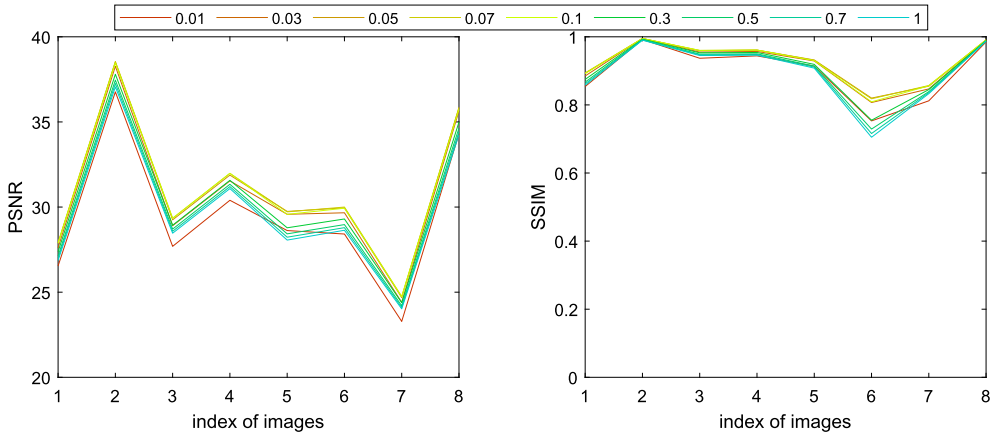

Fig. 7. The PSNR and SSIM values obtained by the proposed LRQR-SR algorithm using different λ with other parameters fixed and SR = 0.5.

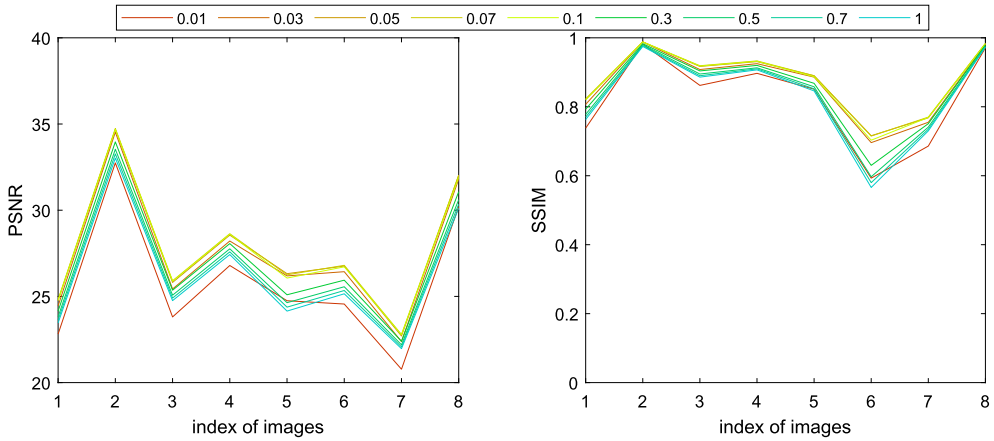

Fig. 8. The PSNR and SSIM values obtained by the proposed LRQR-SR algorithm using different λ with other parameters fixed and SR = 0.3.

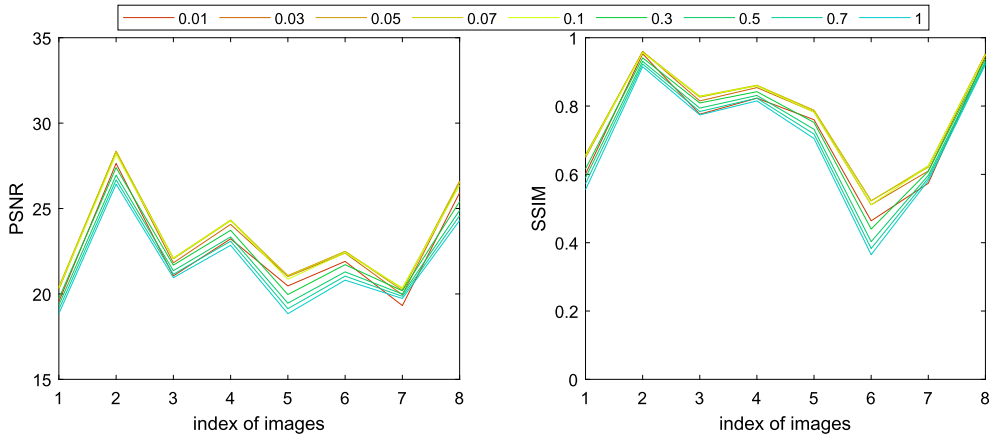

Fig. 9. The PSNR and SSIM values obtained by the proposed LRQR-SR algorithm using different λ with other parameters fixed and SR = 0.1.

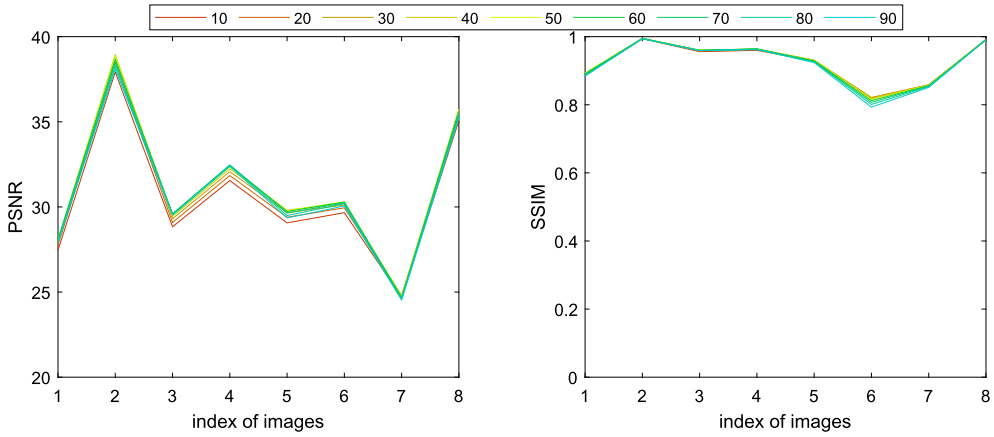

Fig. 10. The PSNR and SSIM values obtained by the proposed LRQR-SR algorithm using different rank with other parameters fixed and SR = 0.5.

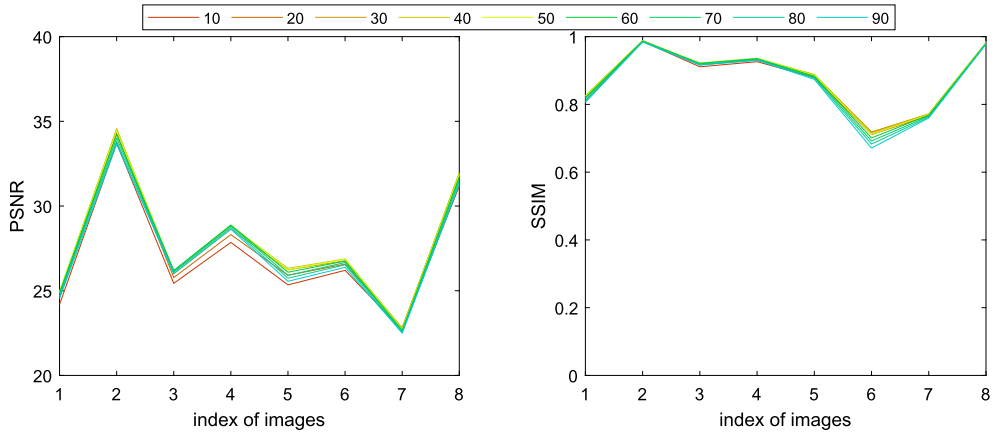

Fig. 11. The PSNR and SSIM values obtained by the proposed LRQR-SR algorithm using different rank with other parameters fixed and SR = 0.3.

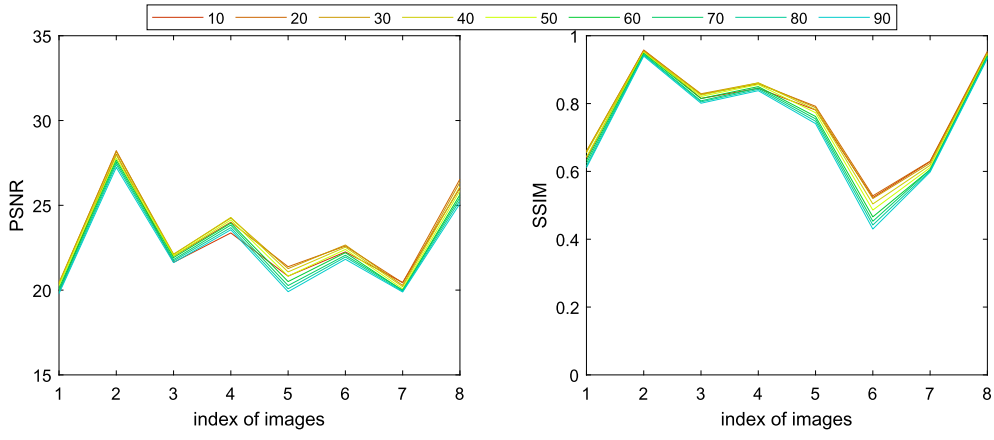

Fig. 12. The PSNR and SSIM values obtained by the proposed LRQR-SR algorithm using different rank with other parameters fixed and SR = 0.1.

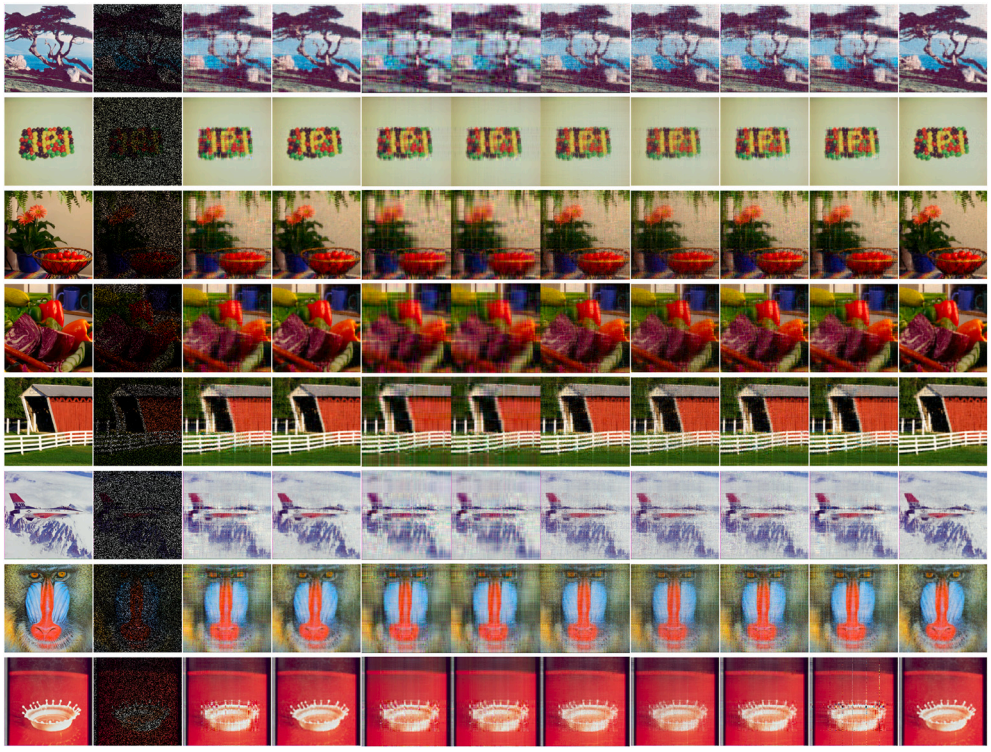

Fig. 13. The first column shows the original image, the second column the observed image (SR = 0.2), and the third to eleventh columns the completion results of TNNR, TNN-SR, D-N, F-N, LRQA, Q-FFN, Q-DNN, QTNN, and LRQR-SR, respectively.

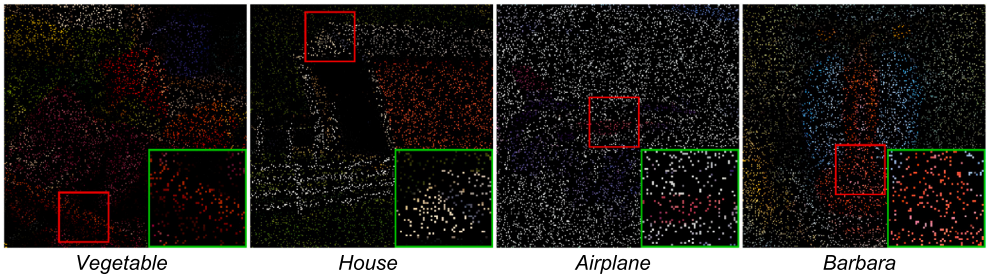

Fig. 14. The enlargement of observed images under SR = 0.1.

Algorithm 2 ADMM solver for problem (17) in Step 2.

Input: $\dot{\mathbf{O}}$, Ω, $\dot{\mathbf{A}}_l$, $\dot{\mathbf{B}}_l$, tolerance ε, and parameters λ, ρ, $\beta_{\max}$.

1: **Initial** $\dot{\mathbf{X}}^1 = \dot{\mathbf{O}}$, $\dot{\mathbf{H}}^1 = \dot{\mathbf{D}}^1 = \dot{\mathbf{X}}^1$, and β^1. Let $\dot{\mathbf{Y}}^1$ and $\dot{\mathbf{Z}}^1$ be random quaternion matrix with the same size of $\dot{\mathbf{X}}^1$.
2: **Repeat**
3: Update $\dot{\mathbf{X}}^{p+1}$
$\dot{\mathbf{X}}^{p+1} = \mathfrak{D}_{\frac{1}{2\beta^p}}(\frac{1}{2}[\dot{\mathbf{H}}^p + \dot{\mathbf{Y}}^p/\beta^p + \mathcal{I}\mathcal{T}(\dot{\mathbf{D}}^p + \dot{\mathbf{Z}}^p/\beta^p)])$.
4: Update $\dot{\mathbf{D}}^{p+1} = \mathcal{S}_{\frac{4\lambda}{\beta^p}}(\mathcal{T}(\dot{\mathbf{X}}^{p+1}) - \dot{\mathbf{Z}}^{pH}/\beta^p)$.
5: Update $\dot{\mathbf{H}}^{p+1} = \dot{\mathbf{X}}^{p+1} + \dot{\mathbf{Y}}^p/\beta^p + \dot{\mathbf{A}}^H\dot{\mathbf{B}}/\beta^p$,
$\dot{\mathbf{H}}^{p+1} = P_{\Omega^C}(\dot{\mathbf{H}}^{p+1}) + P_{\Omega}(\dot{\mathbf{O}})$.
6: Update $\dot{\mathbf{Y}}^{p+1} = \dot{\mathbf{Y}}^p + \beta^p(\dot{\mathbf{X}}^{p+1} - \dot{\mathbf{H}}^{p+1})$.
7: Update $\dot{\mathbf{Z}}^{p+1} = \dot{\mathbf{Z}}^p + \beta^p(\dot{\mathbf{D}}^{p+1} - \mathcal{T}(\dot{\mathbf{X}}^{p+1}))$.
8: Update $\beta^{p+1} = \min\{\rho\beta^p, \beta_{\max}\}$,.
9: **Until convergence** $\|\dot{\mathbf{X}}^{p+1} - \dot{\mathbf{X}}^p\|_F \le \varepsilon$ or p reaches the set maximum iteration number.

Output: $\dot{\mathbf{X}}^{p+1}$.

4.1. Computational complexity

In the analysis of the LRQR-SR model, we examine the computational complexity of the algorithm. Given an input quaternion matrix $\dot{\mathbf{O}} \in \mathbb{H}^{M\times N}$, the computational complexity in **step 1** can be expressed as $\mathcal{O}(\min(M^2N, MN^2))$. Assuming that the solution is obtained from (22), which yields a reduced quaternion matrix of rank r_1, and considering a truncation parameter t, the following complexity is observed: In **step 2**, the computational complexity of the algorithm can be determined by updating $\dot{\mathbf{X}}$, $\dot{\mathbf{D}}$, and $\dot{\mathbf{H}}$ individually. For the update of $\dot{\mathbf{X}}$, the complexity is $\mathcal{O}(\min(M^2N, MN^2) + MNr_1)$. For the update of $\dot{\mathbf{D}}$, the complexity is $\mathcal{O}(M^2N^2)$. As for $\dot{\mathbf{H}}$, the complexity is $\mathcal{O}(MNt)$. Therefore, the overall computational cost of the LRQR-SR model for each iteration is given by $\mathcal{O}(\min(M^2N, MN^2) + MNr_1 + M^2N^2 + MNt)$.

5. Experimental results

5.1. Experimental settings

5.1.1. Comparison methods

Several relevant existing algorithms were used as comparison algorithms, including TNNR [35], TNN-SR [27], D-N and F-N [36], LRQA [4], Q-DNN and Q-FNN [5], QTNN [26]. The comparison of these methods are listed in Table 1.

5.1.2. Test data and experimental environment

All the test images are initially represented by 3-way tensors $\mathcal{T} \in \mathbb{R}^{M\times N\times 3}$. For quaternion-based method, every image is represented by a pure quaternion matrix as $\dot{\mathbf{O}} = \mathbf{O}_R i + \mathbf{O}_G j + \mathbf{O}_B k \in \mathbb{H}^{M\times N}$. All the

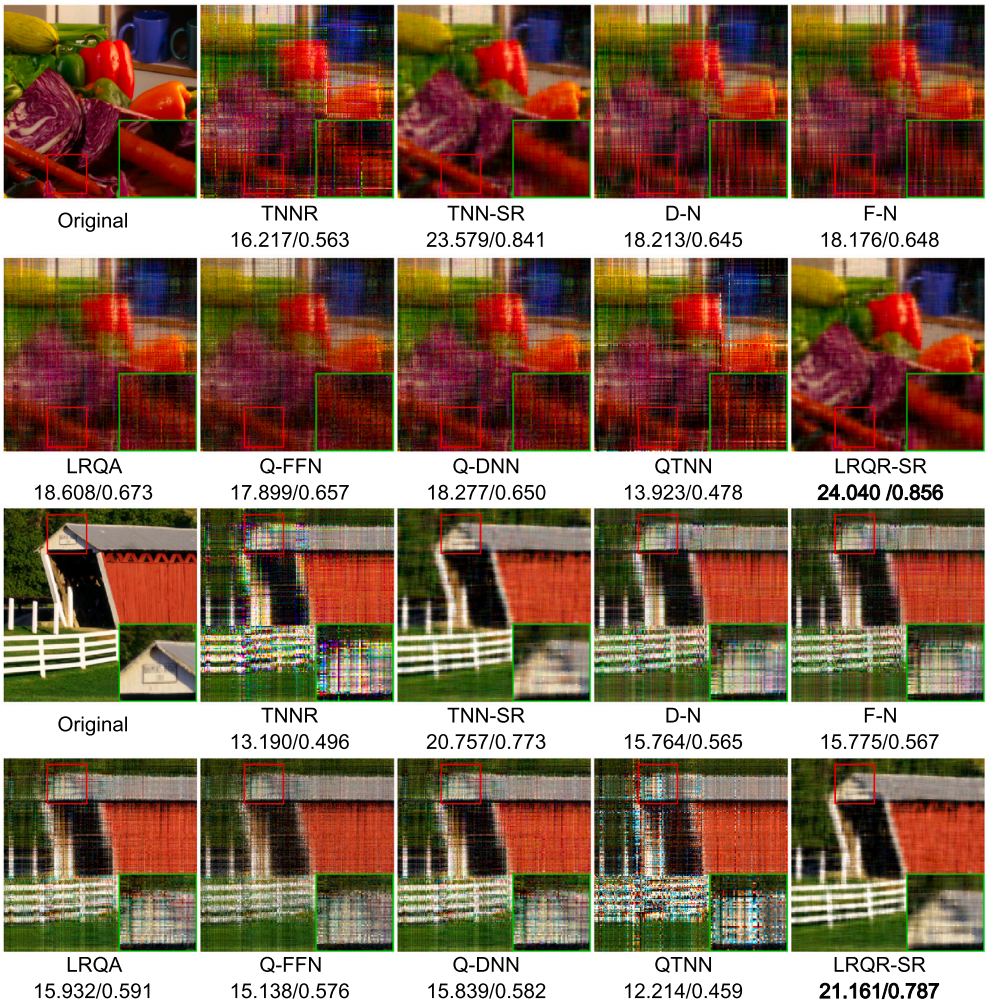

Fig. 15. The recovered results of image $Vegetable$ and $House$ by different methods under SR $= 0.1$.

Table 1
The comparison of the related methods.

Method	Representation of image	Description of low-rankness	Other prior information	Computational complexity
TNNR [35]	matrix-based	truncated nuclear norm	-	$\mathcal{O}(MN\min(M,N))$
TNN-SR [27]	matrix-based	truncated nuclear norm	sparse regularization based on DCT	$\mathcal{O}(MN\min(M,N))$
D-N/ F-N [36]	matrix-based	low-rank matrix factorization	-	$\mathcal{O}(MNd)$
LRQA [4]	quaternion matrix-based	the Laplace, Geman, and weighted Schatten-r functions	-	$\mathcal{O}(MN\min(M,N))$
Q-DNN/ Q-FNN [5]	quaternion matrix-based	low-rank quaternion matrix factorization	-	$\mathcal{O}(MNd)$
QTNN [26]	quaternion matrix-based	truncated nuclear norm	-	$\mathcal{O}(MN\min(M,N))$
LRQR-SR	**quaternion matrix-based**	**truncated nuclear norm**	**sparse regularization based on QDCT**	$\mathcal{O}(MN\min(M,N))$

experiments were implemented in MATLAB R2019a, on a PC with a 3.00 GHz CPU and 8 GB RAM.

Eight benchmark color images as shown in Fig. 3, were selected from SIPI Image Database[1] and McMaster Dataset to demonstrate the effectiveness of the method. In order to fully demonstrate this effectiveness, 50 color images were also randomly selected from Berkeley Segmentation Dataset (BSD)[2] as further test samples.

[1] http://sipi.usc.edu/database/database.php.

[2] Available: https://www2.eecs.berkeley.edu/Research/Projects/CS/vision/bsds/.

5.1.3. Evaluation index setting

The peak signal to noise rate (PSNR) and the structural similarity index (SSIM) were utilized as the relevant quality indexes as they used in the other competitive approaches, which are defined as follows:

$$\mathrm{PSNR} = 10\log 10\left(\frac{\mathrm{Peakval}^2}{\mathrm{MSE}}\right),$$

where Peakval is the maximum possible pixel value in the test image (*e.g.*, for unit8 image it is 255), and MSE is Mean Squared Error, which is calculated as $\mathrm{MSE} = 10\log 10\left(\frac{\|\mathcal{X}-\mathcal{T}\|_F}{MN}\right)$, where $\mathcal{X}$ and $\mathcal{T}$ are the recovered and original images.

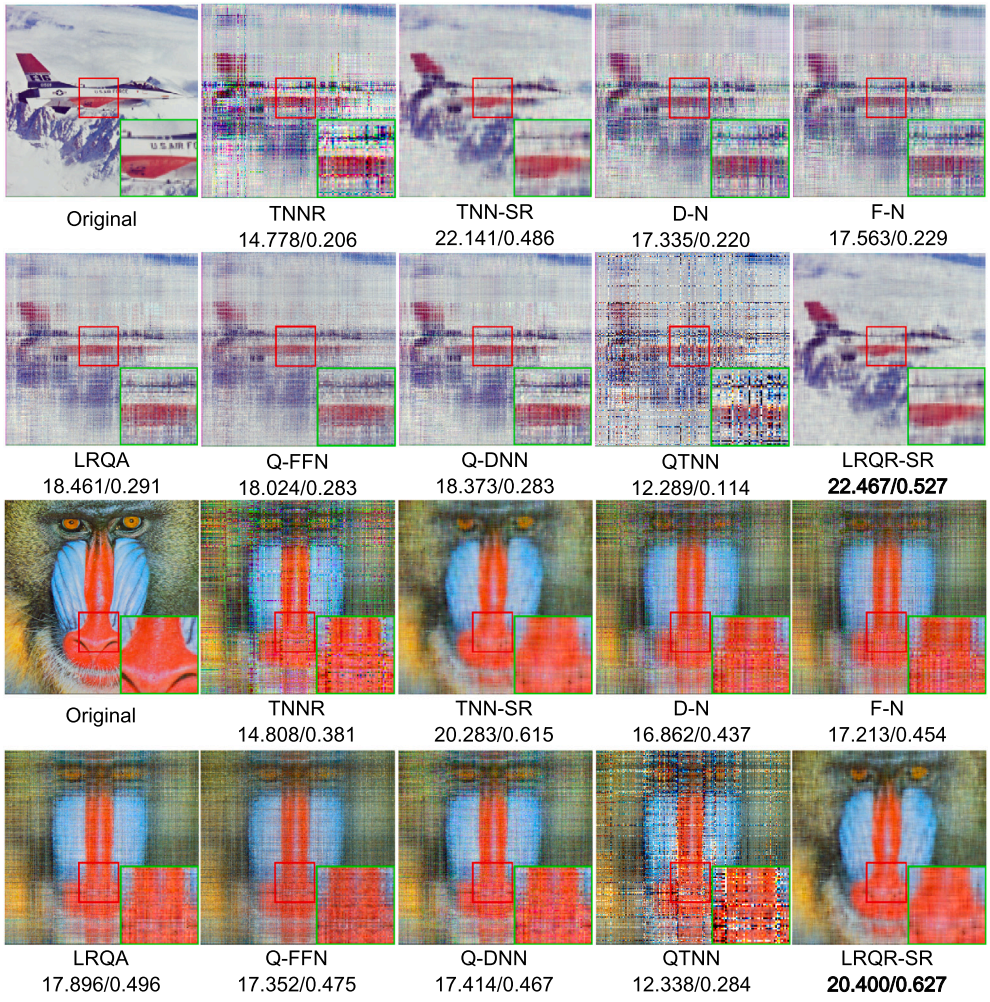

Fig. 16. The recovered results of image *Airplane* and *Barbara* by different methods under SR = 0.1.

$$\text{SSIM} = \frac{(2\mu_{\mathcal{T}}\mu_{\mathcal{X}} + C_1)(2\sigma_{\mathcal{T}\mathcal{X}} + C_2)}{(\mu_{\mathcal{T}^2} + \mu_{\mathcal{X}^2} + C_1)(\sigma_{\mathcal{T}^2} + \sigma_{\mathcal{X}^2} + C_2)},$$

where $\mu_{\mathcal{T}}, \mu_{\mathcal{X}}, \sigma_{\mathcal{T}}, \sigma_{\mathcal{X}}$ and $\sigma_{\mathcal{T}\mathcal{X}}$ are the sample means, variances, and the covariance of images $\mathcal{T}$ and $\mathcal{X}$, $C_1 = (0.01L)^2$, $C_2 = (0.03L)^2$, L is the dynamic range of the pixel values.

The best numerical results are highlighted in **bold** font. When processing image recovery with random samples, a larger Sample Rate (SR) value means more observed pixels in a given image.

5.2. Color image recovery

5.2.1. Simulations with different parameters

As simulations with different settings of the parameters (β^1, λ truncated number r) offer different performance levels, a range of parameters was used to test the performance of the proposed LRQR-SR algorithm, based on recovering random sampled images from Fig. 3.

The influence of different parameter values ($\beta^1 = \{1e-4, 5e-4, 1e-3, 5e-3, 1e-2, 5e-2, 1e-1, 5e-1\}$) on the experimental results was first tested with the other parameters fixed ($\lambda = 0.1, r = 30, \rho = 1.01$) and SR $= \{0.5, 0.3, 0.1\}$. The relevant PSNR and SSIM results are plotted in Fig. 4-6, showing that when $\beta^1 \geq 1e-2$ the recovery effect is minimal. The best recovery results are obtained with different degrees of sampling when $\beta^1 = 1e-4$.

The effect of different parameter values ($\lambda = \{0.01, 0.03, 0.05, 0.07, 0.1, 0.3, 0.5, 0.7, 1\}$) on the recovery results was then tested with other parameters fixed ($\beta^1 = 1e-4, r = 30, \rho = 1.01$) and SR $= \{0.5, 0.3, 0.1\}$. In Fig. 7-9, the relevant PSNR and SSIM values are given, showing that if the value of λ is too large or too small, a better recovery results cannot be obtained. The best recovery results are obtained with different SRs when $\lambda = 0.07$.

Finally, the effect of the number of truncations on the recovery effect was verified. The truncated number r was set as $r = \{10, 20, 30, 40, 50, 60, 70, 80, 90\}$ with other parameters fixed ($\beta^1 = 1e-4, \lambda = 0.07, \rho = 1.01$) and SR $= \{0.5, 0.3, 0.1\}$. In Fig. 10-12, the relevant PSNR and SSIM values are given, indicating that the best recovery results were obtained when the degree of sampling was high (SR $= 0.5$) and the truncated number $r = \{40, 50\}$. However, when the degree of sampling is lower (SR $= \{0.3, 0.1\}$) and $r = \{30, 40\}$, good recovery results are also obtained. This is also consistent with the fact that the more missing pixels in the observed image, the more low-rank constraints are required to improve the recovery effect. Intuitively, when the observed image is missing a lot of pixels, the truncation would contain less useful information.

5.2.2. Images recovery with random sample

The LRQR-SR algorithm was compared with several other methods mentioned previously by setting SR $= \{0.3, 0.2, 0.1\}$. The parameters of LRQR-SR were set as $\beta^1 = 1e-4, \lambda = 0.07, \rho = 1.01$, while the truncation number $r = \{40, 30, 20\}$ was decided by the SR: the lower the SR, the less truncation is required.

Fig. 13 displays the visual comparisons between the designed novel LRQR-SR method and the other methods of comparison for the eight tested color images when SR $= 0.2$. The PSNR and SSIM results of recovery as seen in Fig. 3 with SR $= \{0.3, 0.2, 0.1\}$ are presented in Table 2.

Fig. 17. The recovered results of image *Tree* and *Beans* by different methods under text mask.

As demonstrated, when comparing with other matrix-based methods across all SR values, the results obtained by D-N and F-N do not exhibit significant recovery. However, the effectiveness of factorization techniques becomes more apparent when applied in the quaternion domain, as observed in Q-FFN and Q-DNN. These results serve as evidence for the validity of quaternion-based methods. Additionally, the results of TNNR are inferior to those of TNNR-SR, indicating that relying solely on low-rankness as a prior is insufficient for achieving more accurate image recovery. This supports the rationale behind incorporating sparsity into the LRQR-SR method.

In comparison with other quaternion-based methods, the LRQR-SR method has been found to provide the most visually optimal results, with crisp details. This method outperforms other comparators such as LRQA, Q-FFN, and Q-DNN in terms of both PSNR and SSIM values. The superiority of LRQR-SR can be observed in the data presented in Table 2. When the value of SR is very low, utilizing only the truncated skill cannot accurately recover the potential images. However, LRQR-SR consistently outperforms other methods, demonstrating its effectiveness in achieving high-quality results.

Fig. 15-16 compare the visual results for all the competing completion approaches related to recovering $Vegetable$, $House$, $Airplane$, $Barbara$ under SR $= 0.1$. The corresponding observed images are shown in Fig. 14. The image in the green box is the zoomed-in image of that in the red box. These images demonstrate that solely relying on low rankness for recovery may result in the loss of some local details. However, the proposed method in this study is able to recover more details, such as the outlines and borders of the house and vegetable. On the other hand, approaches like TNNR and QTNN only provide rough restorations when the sample rate is low, and other methods also face similar issues. When comparing the two optimal algorithms, TNN-SR and LRQR-SR, the visual difference in the restored images may not be apparent. However, the corresponding PSNR and SSIM values confirm the superiority of the proposed method.

5.2.3. *Images recovery under text mask*

The LRQR-SR algorithm was then compared with other methods under a text mask. The parameters of LRQR-SR were set to $\beta^1 = 1e-4$, $\lambda = 0.07$, $\rho = 1.01$, and the truncated number $r = 30$.

Fig. 17-18 compares the visual results for all the competing completion approaches related to recovering $Tree$, $Beans$, $Flower$, $Splash$ under text mask. The image in the green box is a zoomed-in image of that in the red box. As shown, the recovered results from D-N and F-N are very blurry, especially in complex image content. This can also be observed from the zoomed-in portion of Fig. 17 ($Tree$) that the results for TNNR, LRQA, Q-FFN, and Q-DNN still leave some obvious artifacts in the blue area. Similar problems can be seen in Fig. 17 ($Beans$). In Fig. 18, there are some obvious artifacts on the red beans in the zoomed-in portion, while in Fig. 18 ($Flower$), some vertical lines remain in the enlarged area after the restoration of the image. In Fig. 18 ($Splash$), some further visible blemishes appear on the white part of the zoomed-in portion. In comparison, the TNNR-SR and the proposed LRQR-SR approaches show better performance. Although there may not be much difference between the two approaches based on visual observation, the

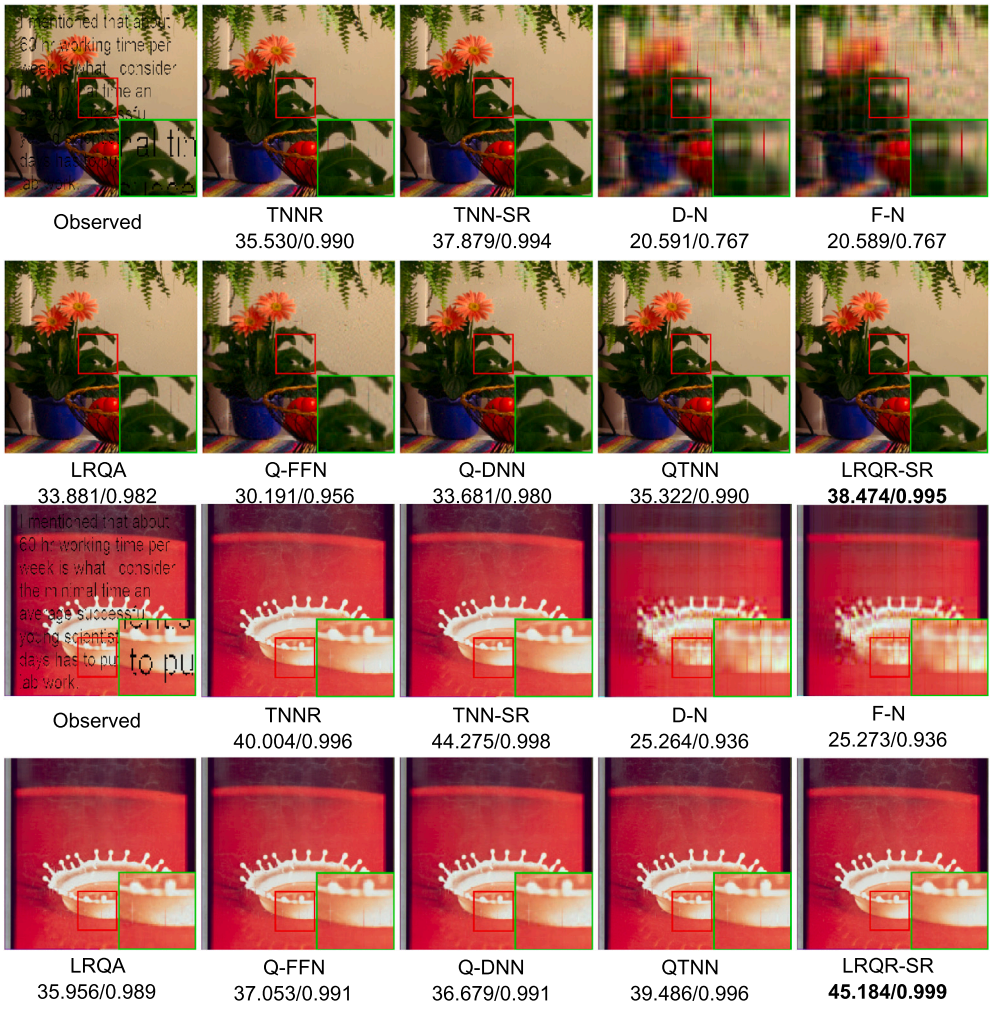

Fig. 18. The recovered results of image $Vegetable$ and $Splash$ by different methods under text mask.

corresponding PSNR and SSIM results indicate that the proposed method can technically restore the image more effectively.

5.2.4. 50 images recovery to further demonstrate the effectiveness of our method

A set of 50 images was subject to recovery to further demonstrate the effectiveness of the method. In this simulation, 50 images were randomly selected from BSD as a test sample, though in order to keep the parameters of the comparison algorithms as in the original set, these images were resized to $256 \times 256 \times 3$ throughout under random sample (SR = 0.25).

The corresponding PSNR and SSIM results are reported in Fig. 19 and Fig. 20. As shown in Fig. 19 and Fig. 20, the effectiveness of sparsity is further demonstrated by the results of TNN-SR and the proposed LRQR-SR. Additionally, when comparing TNN-SR with LRQR-SR, LRQR-SR is found to be superior in all cases. These findings suggest that LRQR-SR outperforms TNN-SR in terms of effectiveness. The proposed LRQR-SR method shows better results in achieving sparsity, indicating its potential for more efficient and accurate data representation.

5.3. Discussions

The simulation experiment results offer various items for discussion that can be summarized as follows:

- The newly-developed LRQR-SR algorithm outperforms comparable existing algorithms both visually and numerically. The main reasons for this can be summarized in three points: this algorithm has been developed in the quaternion domain where the spatial structure information of color image is not destroyed; the model uses QTNN to depict low-rankness, which helps preserve the information contained in the first few large singular values; and, finally, the l_1 norm is added to act as the regularization in the algorithm, helping to model the sparseness of the underlying quaternion matrix.
- When compared with matrix-based methods, TNNR, D-N, and F-N only depict low-rankness by means of modified NN or low-rank factorization. Hence, the recovery results are generally not satisfactory. However, as TNN-SR is based on both low-rankness and sparse priors, the recovered results are improved. In general, for matrix-based methods, the RGB channels of color images must be processed separately causing the recovered color images to potentially have details omitted.
- When compared with quaternion matrix-based methods, LRQA, Q-FFN, Q-DNN, and QTNN are limited by only utilizing low-rankness. For LRQR-SR, the l_1 norm is also incorporated to describe the sparse prior of the underlying quaternion matrix in the QDCT domain. Thus, LRQR-SR offers superior performance to the other comparable methods.

6. Conclusion

This paper introduces a novel approach for low-rank quaternion recovery with sparse regularization, enhancing both the theoretical under-

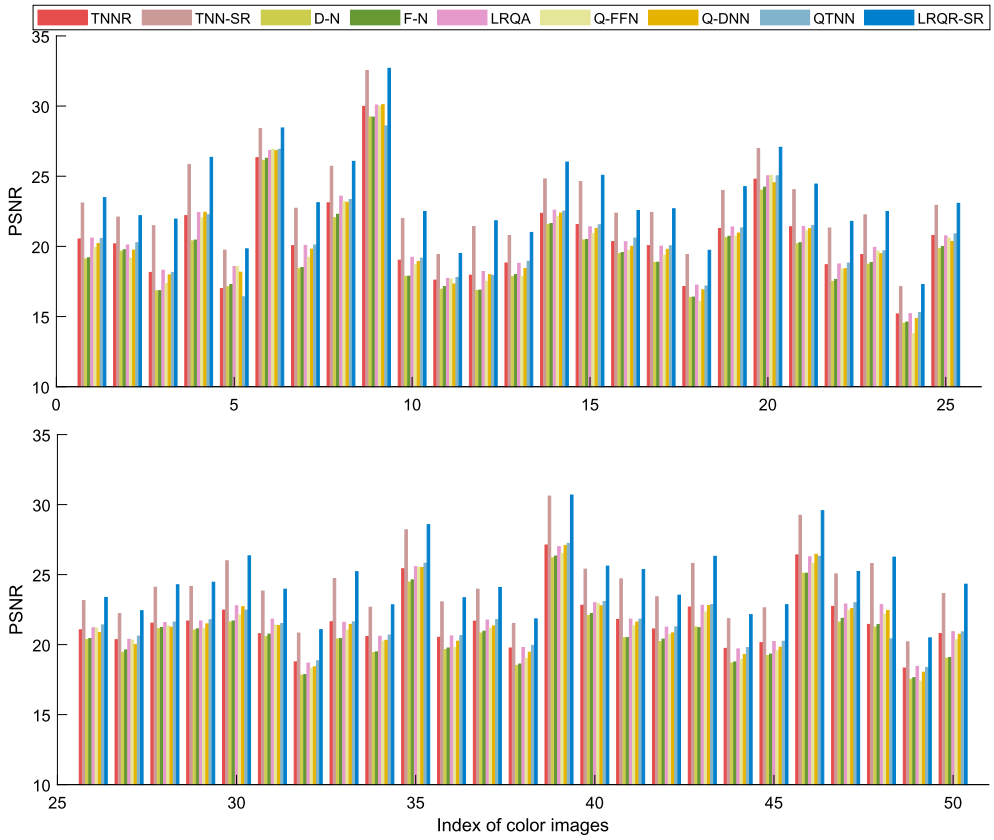

Fig. 19. Comparison of the PSNR results of different algorithms for recovering 50 color images selected from BSD (SR = 0.25).

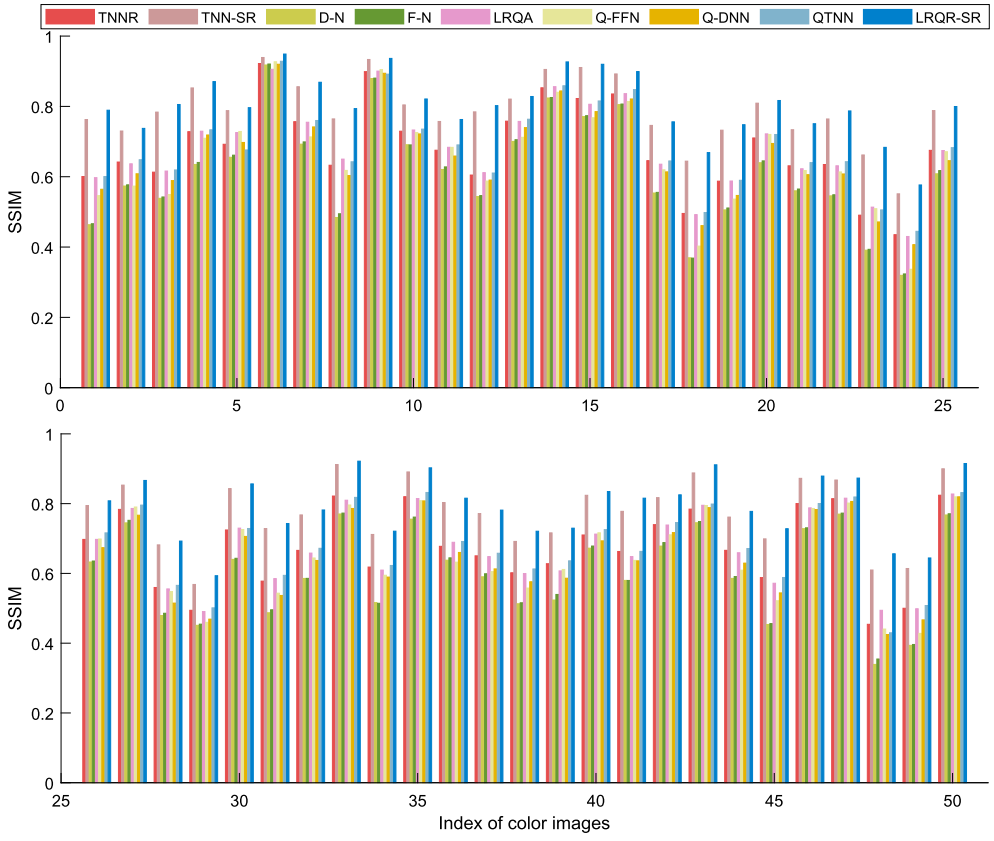

Fig. 20. Comparison of the SSIM results of different algorithms for recovering 50 color images selected from BSD (SR = 0.25).

Table 2
The PSNR/SSIM values obtained by different recovery algorithms for 8 color images.

Image	SR = 0.3								
	TNNR [35]	TNN-SR [27]	D-N [36]	F-N [36]	LRQA [4]	Q-FFN [5]	Q-DNN [5]	QTNN [26]	LRQR-SR
Tree	20.936/0.670	23.275/0.793	18.356/0.490	18.309/0.485	21.148/0.668	20.600/0.650	21.070/0.657	21.028/0.676	**24.915/0.827**
Beans	27.699/0.954	33.799/0.984	26.509/0.938	26.559/0.938	27.950/0.950	28.100/0.957	28.133/0.955	28.324/0.960	**34.583/0.988**
Flower	22.275/0.818	25.343/0.903	20.061/0.735	20.093/0.738	22.353/0.816	22.053/0.796	22.260/0.807	22.588/0.830	**26.128/0.920**
Vegetable	24.053/0.848	27.861/0.919	20.871/0.757	20.861/0.758	24.294/0.854	24.002/0.852	24.311/0.848	24.359/0.859	**28.865/0.936**
House	21.838/0.802	25.357/0.873	19.299/0.711	19.288/0.712	22.162/0.804	21.786/0.786	22.281/0.799	21.866/0.806	**26.272/0.887**
Airplane	23.182/0.544	26.237/0.676	21.028/0.400	21.078/0.399	23.101/0.527	22.777/0.526	23.059/0.518	23.214/0.548	**26.851/0.712**
Barbara	20.853/0.690	22.525/0.758	19.992/0.590	20.038/0.591	20.688/0.679	19.433/0.603	20.065/0.643	21.046/0.697	**22.734/0.769**
Splash	26.761/0.952	31.508/0.979	24.838/0.933	24.938/0.934	26.926/0.951	26.699/0.950	27.124/0.951	26.860/0.952	**32.126/0.982**
Image	SR = 0.2								
	TNNR [35]	TNN-SR [27]	D-N [36]	F-N [36]	LRQA [4]	Q-FFN [5]	Q-DNN [5]	QTNN [26]	LRQR-SR
Tree	18.517/0.545	21.921/0.730	17.465/0.433	17.551/0.447	18.910/0.551	18.354/0.515	18.554/0.523	18.583/0.548	**23.093/0.769**
Beans	24.163/0.918	31.165/0.974	24.846/0.918	24.990/0.918	25.103/0.924	25.018/0.926	25.197/0.927	25.033/0.930	**31.804/0.979**
Flower	20.112/0.736	23.599/0.866	19.214/0.692	19.310/0.698	20.442/0.745	20.068/0.725	20.062/0.719	20.465/0.753	**24.138/0.884**
Vegetable	21.674/0.781	25.978/0.891	20.299/0.732	20.299/0.735	21.947/0.791	21.902/0.790	21.737/0.777	22.028/0.796	**26.802/0.909**
House	19.232/0.723	23.615/0.839	18.423/0.677	18.397/0.677	19.800/0.736	18.950/0.710	19.464/0.716	19.120/0.727	**24.349/0.855**
Airplane	20.601/0.419	24.496/0.600	19.641/0.332	19.774/0.340	20.898/0.421	20.401/0.400	20.608/0.404	20.739/0.427	**25.002/0.636**
Barbara	19.335/0.602	21.487/0.697	18.935/0.547	19.174/0.554	19.503/0.601	19.301/0.593	18.884/0.567	19.522/0.609	**21.695/0.710**
Splash	24.285/0.929	29.473/0.970	23.620/0.919	23.689/0.920	24.643/0.931	24.211/0.929	24.643/0.929	23.946/0.924	**29.915/0.973**
Image	SR = 0.1								
	TNNR [35]	TNN-SR [27]	D-N [36]	F-N [36]	LRQA [4]	Q-FFN [5]	Q-DNN [5]	QTNN [26]	LRQR-SR
Tree	13.794/0.256	19.943/0.629	14.905/0.266	15.232/0.289	15.893/0.364	15.474/0.359	15.604/0.338	11.508/0.178	**20.435/0.657**
Beans	17.403/0.779	28.089/0.952	21.672/0.845	21.777/0.846	22.191/0.879	22.293/0.869	22.135/0.879	14.141/0.388	**28.511/0.960**
Flower	14.956/0.467	21.673/0.807	16.960/0.564	17.195/0.583	17.973/0.632	17.457/0.615	17.541/0.595	12.518/0.346	**22.013/0.825**
Vegetable	16.217/0.563	23.579/0.841	18.213/0.645	18.176/0.648	18.608/0.673	17.899/0.657	18.277/0.650	13.923/0.478	**24.040/0.856**
House	13.190/0.496	20.757/0.773	15.764/0.565	15.775/0.567	15.932/0.591	15.138/0.576	15.839/0.582	12.214/0.459	**21.161/0.787**
Airplane	14.778/0.206	22.141/0.486	17.335/0.220	17.563/0.229	18.461/0.291	18.024/0.283	18.373/0.283	12.289/0.114	**22.467/0.527**
Barbara	14.808/0.381	20.283/0.615	16.862/0.437	17.213/0.454	17.896/0.496	17.352/0.475	17.414/0.467	12.338/0.284	**20.400/0.627**
Splash	16.765/0.817	26.556/0.948	20.228/0.884	20.299/0.886	21.157/0.891	20.616/0.890	21.015/0.885	13.311/0.737	**26.900/0.953**

standing and practical application of quaternion matrix recovery techniques. By integrating low-rank and sparse regularization, this method extends existing techniques and offers a more comprehensive framework for recovering quaternion matrices. The combination of low-rank and sparse structures in the recovery model bridges the gap between these two crucial properties, advancing the understanding of their relationship in quaternion matrices. This approach not only improves data recovery accuracy but also provides practical advantages. However, it is necessary to consider limitations such as computational complexity and parameter sensitivity. Future research should focus on developing more robust sparse representations through deep learning [37], incorporating additional prior knowledge for more efficient recovery, and creating scalable algorithms for high-resolution image processing [38].

Declaration of competing interest

The authors declare that they have no known competing financial interests or personal relationships that could have appeared to influence the work reported in this paper.

Data availability

Data will be made available on request.

Acknowledgments

This work is supported by University of Macau (MYRG2022-000108-FST) and (MYRG-CRG2022-00010-ICMS), and the National Natural Science Foundation of China (Grant No. 62173308), and the Natural Science Foundation of Zhejiang Province of China (Grant No. LR20F030001), and the Jinhua Science and Technology Project (Grant No. 2022-1-042).

References

[1] Henry Shaowu Yuchi, Simon Mak, Yao Xie, Bayesian uncertainty quantification for low-rank matrix completion, Bayesian Anal. 18 (2) (2023) 491–518.
[2] Pengling Wu, Kit Ian Kou, Jifei Miao, Efficient low-rank quaternion matrix completion under the learnable transforms for color image recovery, Appl. Math. Lett. 148 (2024) 108880.
[3] Mingcui Zhang, Wenxv Ding, Ying Li, Jianhua Sun, Zhihong Liu, Color image watermarking based on a fast structure-preserving algorithm of quaternion singular value decomposition, Signal Process. 208 (2023) 108971.
[4] Yongyong Chen, Xiaolin Xiao, Yicong Zhou, Low-rank quaternion approximation for color image processing, IEEE Trans. Image Process. 29 (2020) 1426–1439.
[5] Jifei Miao, Kit Ian Kou, Quaternion-based bilinear factor matrix norm minimization for color image inpainting, IEEE Trans. Signal Process. 68 (2020) 5617–5631.
[6] Ricardo Silveira Cabral, Fernando De la Torre, João Paulo Costeira, Alexandre Bernardino, Unifying nuclear norm and bilinear factorization approaches for low-rank matrix decomposition, in: 2013 IEEE International Conference on Computer Vision, 2013, pp. 2488–2495.
[7] Jiabao Li, Yuqi Li, Chong Wang, Xulun Ye, Wolfgang Heidrich, Busifusion: blind unsupervised single image fusion of hyperspectral and RGB images, IEEE Trans. Comput. Imaging 9 (2023) 94–105.
[8] John Wright, Yi Ma, Julien Mairal, Guillermo Sapiro, Thomas S. Huang, Shuicheng Yan, Sparse representation for computer vision and pattern recognition, Proc. IEEE 98 (6) (2010) 1031–1044.
[9] Jun Lang, Changchun Zhang, Di Zhu, Undersampled MRI reconstruction based on spectral graph wavelet transform, Comput. Biol. Med. 157 (2023) 106780.
[10] Xiaoyu Zhao, Xiaoqian Chen, Zhiqiang Gong, Weien Zhou, Wen Yao, Yunyang Zhang, Recfno: a resolution-invariant flow and heat field reconstruction method from sparse observations via Fourier neural operator, Int. J. Therm. Sci. 195 (2024) 108619.
[11] Yongjun Zhang, Zewei Wang, Xuexue Zhang, Zhongwei Cui, Bob Zhang, Jinrong Cui, Lamin L. Janneh, Application of improved virtual sample and sparse representation in face recognition, CAAI Trans. Intell. Technol. 8 (4) (2023) 1391–1402.
[12] John Wright, Allen Y. Yang, Arvind Ganesh, Shankar S. Sastry, Yi Ma, Robust face recognition via sparse representation, IEEE Trans. Pattern Anal. Mach. Intell. 31 (2) (2009) 210–227.
[13] Wei Yuan, Han Liu, Lili Liang, Joint group dictionary-based structural sparse representation for image restoration, Digit. Signal Process. 137 (2023) 104029.
[14] Jun Xu, Lei Zhang, David Zhang, A trilateral weighted sparse coding scheme for real-world image denoising, in: Computer Vision - ECCV 2018 - 15th European Conference, Proceedings, Part VIII, Munich, Germany, September 8–14, 2018, in: Lecture Notes in Computer Science, vol. 11212, Springer, 2018, pp. 21–38.

[15] Xiang Chen, Hao Li, Mingqiang Li, Jinshan Pan, Learning A sparse transformer network for effective image deraining, in: IEEE/CVF Conference on Computer Vision and Pattern Recognition, CVPR 2023, Vancouver, BC, Canada, June 17–24, 2023, IEEE, 2023, pp. 5896–5905.
[16] Zhiyuan Zha, Bihan Wen, Xin Yuan, Saiprasad Ravishankar, Jiantao Zhou, Ce Zhu, Learning nonlocal sparse and low-rank models for image compressive sensing: nonlocal sparse and low-rank modeling, IEEE Signal Process. Mag. 40 (1) (2023) 32–44.
[17] Xiao Liang, Xiang Ren, Zhengdong Zhang, Yi Ma, Repairing sparse low-rank texture, in: Computer Vision - ECCV 2012 - 12th European Conference on Computer Vision, Proceedings, Part V, Florence, Italy, October 7–13, 2012, in: Lecture Notes in Computer Science, Springer, 2012, pp. 482–495.
[18] Yulong Wang, Kit Ian Kou, Cuiming Zou, Yuan Yan Tang, Robust sparse representation in quaternion space, IEEE Trans. Image Process. 30 (2021) 3637–3649.
[19] Cuiming Zou, Kit Ian Kou, Yuan Yan Tang, Hao Deng, Adaptive reweighted quaternion sparse learning for data recovery and classification, Pattern Recognit. 142 (2023) 109653.
[20] Zhigang Jia, Michael K. Ng, Guang-Jing Song, Robust quaternion matrix completion with applications to image inpainting, Numer. Linear Algebra Appl. 26 (4) (2019).
[21] William Rowan Hamilton, II. On quaternions; or on a new system of imaginaries in algebra, Lond. Edinb. Dublin Philos. Mag. J. Sci. 25 (163) (1844) 10–13.
[22] Nicolas Le Bihan, Jérôme I. Mars, Singular value decomposition of quaternion matrices: a new tool for vector-sensor signal processing, Signal Process. 84 (7) (2004) 1177–1199.
[23] Fuzhen Zhang, Quaternions and matrices of quaternions, Linear Algebra Appl. 251 (1997) 21–57.
[24] Yibin Yu, Yulan Zhang, Shifang Yuan, Quaternion-based weighted nuclear norm minimization for color image denoising, Neurocomputing 332 (2019) 283–297.
[25] Nicolas Le Bihan, Stephen J. Sangwine, Quaternion principal component analysis of color images, in: Proceedings of the 2003 International Conference on Image Processing, ICIP 2003, Barcelona, Catalonia, Spain, September 14–18, 2003, IEEE, 2003, pp. 809–812.
[26] Liqiao Yang, Kit Ian Kou, Jifei Miao, Weighted truncated nuclear norm regularization for low-rank quaternion matrix completion, J. Vis. Commun. Image Represent. 81 (2021) 103335.
[27] Jing Dong, Zhichao Xue, Jian Guan, Zi-Fa Han, Wenwu Wang, Low rank matrix completion using truncated nuclear norm and sparse regularizer, Signal Process. Image Commun. 68 (2018) 76–87.
[28] Jicong Fan, Tommy W.S. Chow, Matrix completion by least-square, low-rank, and sparse self-representations, Pattern Recognit. 71 (2017) 290–305.
[29] Ce Li, Qiang Ma, Limei Xiao, Ming Li, Aihua Zhang, Image splicing detection based on Markov features in QDCT domain, Neurocomputing 228 (2017) 29–36.
[30] Wei Feng, Bo Hu, Quaternion Discrete Cosine Transform and Its Application in Color Template Matching, 2008 Congress on Image and Signal Processing, vol. 2, IEEE, 2008, pp. 252–256.
[31] Lu Li, Xingyu Wang, Guoqiang Wang, Alternating direction method of multipliers for separable convex optimization of real functions in complex variables, Math. Probl. Eng. (2015) 2015.
[32] Mawardi Bahri, Eckhard S.M. Hitzer, Akihisa Hayashi, Ryuichi Ashino, An uncertainty principle for quaternion Fourier transform, Comput. Math. Appl. 56 (9) (2008) 2398–2410.
[33] Eckhard Hitzer, Quaternion Fourier transform on quaternion fields and generalizations, CoRR, arXiv:1306.1023 [abs], 2013.
[34] Dongpo Xu, Danilo P. Mandic, The theory of quaternion matrix derivatives, IEEE Trans. Signal Process. 63 (6) (2015) 1543–1556.
[35] Yao Hu, Debing Zhang, Jieping Ye, Xuelong Li, Xiaofei He, Fast and accurate matrix completion via truncated nuclear norm regularization, IEEE Trans. Pattern Anal. Mach. Intell. 35 (9) (2013) 2117–2130.
[36] Fanhua Shang, James Cheng, Yuanyuan Liu, Zhi-Quan Luo, Zhouchen Lin, Bilinear factor matrix norm minimization for robust PCA: algorithms and applications, IEEE Trans. Pattern Anal. Mach. Intell. 40 (9) (2018) 2066–2080.
[37] Wen Shen, Zhihua Wei, Qihan Ren, Binbin Zhang, Shikun Huang, Jiaqi Fan, Quanshi Zhang, Interpretable rotation-equivariant quaternion neural networks for 3d point cloud processing, IEEE Trans. Pattern Anal. Mach. Intell. 46 (5) (2024) 3290–3304.
[38] Qinglong Cao, Zhengqin Xu, Chao Ma, Xiaokang Yang, Yuntian Chen, Vision-informed flow image super-resolution with quaternion spatial modeling and dynamic flow convolution, CoRR, arXiv:2401.15913 [abs], 2024.

Liqiao Yang received the M.S. degree in mathematics from University of Electronic Science and Technology of China, Chengdu, in 2020.

She received the Ph.D. degree in mathematics from the University of Macau, China, in 2024.

Her current research interests include quaternion modeling and algorithm for high-order data recovery.

Yang Liu received the B.S. degree in mathematics from Zhejiang Normal University, Zhejiang, China, in 2003, and the Ph.D. degree from Tongji University, Shanghai, China, in 2008. He is currently a Professor with the College of Mathematics and Computer Science and the College of Mathematical Medicine, Zhejiang Normal University. He has authored over 100 publications and two books. His research interests include distributed optimization, hybrid systems, and logical systems. Dr. Liu was recognized by Elsevier as a Most Cited Chinese Researcher in 2020 and Clarivate Analytics as a Highly Cited Researcher in 2019–2021. He is also an Associate Editor of Neural Processing Letters (Springer).

Kit Ian Kou received the Ph.D. degree in mathematics from the University of Macau, Macau, in 2005.

She is currently a Life Member of Clare Hall, University of Cambridge, Cambridge, U.K. She is also an Associate Professor with the Department of Mathematics, Faculty of Science and Technology,

University of Macau. Her current research interests include pattern recognition, quaternion analysis in image processing, Fourier analysis, and sampling theory. Prof. Kou received the Third Prize in the Natural Science Award of 2018 Macao Science and Technology Awards.